Moisture sources and dynamics over the Southeast Tibetan Plateau reflected in dual water vapor isotopes

Zhongyin Cai[1], Rong Li[1], Cheng Wang[1], Qiukai Mao[1], Lide Tian[1]

[1]Institute of International Rivers and Eco-security, Yunnan Key Laboratory of International Rivers and Transboundary Eco-security, State Key Laboratory of Vegetation Structure, Function and Construction (VegLab), Yunnan University, Kunming, 650500, China

Correspondence to: Zhongyin Cai (czypil@gmail.com and z.cai@ynu.edu.cn)

Abstract. The Southeast Tibetan Plateau (SETP) has experienced a significant drying trend in recent decades, which is likely linked to shifts in moisture sources. To investigate the roles of ocean surface evaporation, continental air mass intrusion, and precipitation–vapor interactions, we present a three-year daily time series of near-surface vapor $\delta^{18}O$ and *d*-excess data from the SETP station. Our analysis reveals that apparent negative correlations between *d*-excess and relative humidity over the Indian Ocean are primarily due to anticorrelated seasonal cycles, which become insignificant or marginal when examined seasonally. This result underscores the need for caution in interpreting *d*-excess as a conservative tracer of ocean surface evaporation. Instead, we identify local and upstream specific humidity as the primary determinants of non-monsoon season *d*-excess variability, which is influenced by the intrusion of cold and dry air from upper levels. During the summer monsoon season, both *d*-excess and $\delta^{18}O$ reflect the effect of raindrop evaporation during transport, which decreases $\delta^{18}O$ but increases *d*-excess. These findings offer new insights into the use of water isotopes to track moisture sources and circulation changes across the SETP, especially under varying seasonal circulation systems. In particular, the findings for *d*-excess will contribute to our understanding of shifts in moisture sources and provide a framework for interpreting *d*-excess in various hydroclimatic applications, including ice core studies.

1 Introduction

The Tibetan Plateau (TP) and its surrounding regions, known as the Third Pole and the Asian Water Tower, are critical sources of freshwater for billions of people (Immerzeel et al., 2020; Yao et al., 2022). Recent climate change has induced significant hydrological shifts, marked by drying trends in the Southeast TP (SETP) and wetting in the north (Yao et al., 2022; Jiang et al., 2023; Zhang et al., 2023). Atmospheric water vapor is the primary input to the hydrological system, making it essential to understand its sources and dynamics to diagnose regional water imbalances. Using a Lagrangian vapor tracking method, Zhang et al. (2023) suggested that the drying trend is associated with meteorological droughts propagating from a shift in moisture source regions. However, their conclusions and methodology are subjects of ongoing debate (Zhang et al., 2025; Zhao et al., 2025), underscoring the need for alternative approaches. As natural tracers of the water cycle, water stable isotopes offer

valuable insights into moisture sources and dynamics (Galewsky et al., 2016; Bowen et al., 2019). However, the interpretation of water isotopes on the TP remains challenging because of complex fractionation processes and shifting circulation systems between summer monsoon and westerlies (Yao et al., 2013; Bershaw, 2018; Thompson et al., 2024; Li et al., 2025).

Recent studies have confirmed that monsoon convection at upstream locations along moisture transport pathways, rather than the local precipitation amount, controls summer monsoon season precipitation $\delta^{18}O$ over the southern TP (He et al., 2015; Cai et al., 2017). This is related to the "amount effect" (Dansgaard, 1964), where higher precipitation leads to lower $\delta^{18}O$ values due to continuous rainout associated with stronger convection following the Rayleigh distillation (Kurita et al., 2015; Ruan et al., 2019; Cai et al., 2025). Additionally, interactions between precipitation and water vapor play a significant role in depleting lower tropospheric vapor isotopes (Lee and Fung, 2008; Risi et al., 2008a; Kurita et al., 2011; Cai et al., 2018). Although the regional amount effect prevails during the monsoon season, this relationship weakens or reverses in the non-monsoon season when it is dominated by westerlies. This variability suggests the presence of additional controls, such as moisture source variability, kinetic fractionation, or shifts in atmospheric circulation patterns (Breitenbach et al., 2010; Yao et al., 2013; Cai and Tian, 2020; Guo et al., 2024).

Observations of vapor isotopes could help disentangle the different processes involved in the amount effect, particularly through examining the secondary parameter deuterium excess (*d*-excess). The *d*-excess, defined by Dansgaard (1964) as $\delta^{2}H - 8\delta^{18}O$, primarily reflects the effects of kinetic fractionation. During the rainout process, equilibrium fractionation is the dominant mechanism, whereas raindrop evaporation is associated with kinetic fractionation. Furthermore, limited precipitation during non-monsoon seasons makes it challenging to study a full seasonal cycle of the atmospheric water cycle, which can be compensated for by continuous monitoring of vapor isotopes. Although a few stations on the TP have monitored isotopic compositions in the vapor phase (Yu et al., 2015; Yu et al., 2016; Tian et al., 2020; Dai et al., 2021; Chen et al., 2024), there is limited knowledge about vapor *d*-excess.

Both theoretical predictions and observations over ocean surfaces indicate that *d*-excess reflects ocean surface evaporation conditions, such as sea surface temperature (SST) and relative humidity normalized to SST (RH_{SST}) (Craig and Gordon, 1965; Merlivat and Jouzel, 1979; Liu et al., 2014; Bonne et al., 2019). These relationships are frequently used to interpret *d*-excess values over the TP (Zhao et al., 2012; Shao et al., 2021; Chen et al., 2024; Liu et al., 2024). For example, Shao et al. (2021) reported significant correlations between an ice core *d*-excess record from the central TP and RH_{SST} over the northern Bay of Bengal (BOB) and Arabian Sea (AS). However, the correlation coefficient was only −0.44, with a steep slope of −0.99‰ $\%^{-1}$, which differs from the typical range observed in oceanic regions (−0.3‰ $\%^{-1}$ to −0.6‰ $\%^{-1}$) (Uemura et al., 2008; Benetti et al., 2014; Liu et al., 2014; Bonne et al., 2019). This discrepancy suggests additional complexities, such as continental recycling and raindrop evaporation. Furthermore, many studies at other terrestrial sites have also questioned whether *d*-excess accurately preserves evaporation conditions from oceanic source regions (Welp et al., 2012; Aemisegger et al., 2014; Samuels‐Crow et al., 2014; Fiorella et al., 2018; Wei and Lee, 2019).

In addition, ice core *d*-excess values at high altitudes are generally higher than those observed in precipitation at lower altitudes on the TP (Thompson et al., 2000; Tian et al., 2001; Zhao et al., 2012; Joswiak et al., 2013; Zhao et al., 2017; Shao et al., 2021). High vapor *d*-excess values at high elevations have been observed elsewhere, such as on the Andes (Samuels‐Crow et al., 2014). Such elevated *d*-excess values have been attributed to the mixing with subsiding air (Samuels‐Crow et al., 2014; Sodemann et al., 2017). However, this mechanism remains unconfirmed on the TP.

Mountain valleys in the SETP are considered as significant pathways for transporting water vapor into the TP (Araguás-Araguás et al., 1998; Tian et al., 2007; Yao et al., 2013). To investigate these processes, we initiated a water vapor sampling campaign at the South-East Tibetan Plateau Station for integrated observation and research of alpine environment (SETP station) in June 2015. The primary objectives were to explore moisture sources and dynamics and their influence on vapor isotope compositions across different seasons. To achieve these goals, we analyzed the relationships between vapor isotopes and oceanic evaporation conditions, continental air mass intrusions, and precipitation−vapor interactions during different seasons. Finally, we discuss how our findings contribute to the interpretation of ice core records.

2 Data and methods

2.1 Atmospheric water vapor sampling

Vapor samples were collected at the SETP station (29°46'N, 94°44'E, 3326 m above sea level, and Fig. S1) using a cryogenic trapping method. The sampling system included an air pump, a linked-ball-shaped glass cold trap, and an electric-powered system that creates and maintains a cold environment filled with 95% ethanol as cold as below -80 °C. Ambient air was pumped from an inlet positioned approximately 8 m above ground level through a Teflon tube to a glass trap maintained at an operating temperature of -70 °C. The airflow rate was set to approximately 5 L/min, allowing the collection of 10−20 ml of water samples during each sampling session. The sampling durations were adjusted seasonally: 24 hours in summer and extended to 48 hours in winter when necessary to ensure adequate sample volume. The samples were collected at 20:00 Beijing Standard Time (12:00 UTC). The efficiency of the trapping method was verified by connecting an additional cold trap to the system, which showed no visible condensation in the additional cold trap (Yu et al., 2015). Further validation was achieved through comparisons with direct measurements using a cavity ring-down spectroscopy (CRDS, model Picarro L2130-i) at Lhasa, southern TP, confirming the reliability of this method for atmospheric water vapor sampling (Tian et al., 2020).

The sampling campaign ran from 25 June 2015 to 14 June 2018, yielding a total of 742 samples. These samples were stored frozen until analysis. Those collected before 28 June 2016 were measured at the Key Laboratory of Tibetan Plateau Earth System, Environment and Resources, Institute of Tibetan Plateau Research, Chinese Academy of Sciences, using a Picarro L2130-i analyzer. Samples collected after 28 June 2016 were measured at the Institute of International River and Eco-security, Yunnan University, using a Picarro L2140-i analyzer. The isotopic values were calibrated using three standard water samples,

with the detailed calibration procedures described by Liu et al. (2024). The measurements are expressed relative to Vienna Standard Mean Ocean Water 2 (VSMOW2), with precisions of 0.1‰ for $\delta^{18}O$, 0.4‰ for $\delta^{2}H$, and 1.2‰ for *d*-excess.

2.2 Meteorological data

Daily local meteorological data prior to 2018, including the precipitation amount, air temperature, air pressure, and relative humidity at the SETP station, were obtained from the National Tibetan Plateau/Third Pole Environment Data Center (Luo, 2018). The specific humidity (q) at the SETP station was calculated using air temperature, air pressure, and relative humidity data following the established equations outlined in Huang (2018).

We further obtained meteorological variables such as 2-meter air temperature, 2-meter dew point temperature, SST, and others at 0.25°×0.25° and hourly resolution from the European Centre for Medium-Range Weather Forecasts fifth generation reanalysis (ERA5) (Hersbach et al., 2019). The RH_{SST} is estimated using ERA5 data: $RH_{SST} = e_{air}/e_{sat}$, where e_{air} is the vapor pressure of air and where e_{sat} is the saturation vapor pressure with respect to the SST. Additionally, precipitation data at 0.1°×0.1° and half-hourly resolutions were obtained from the Integrated Multi-satellitE Retrievals for GPM (V07) dataset (Huffman et al., 2023). Moreover, we used ERA5 data and meteorological data at 1°×1° and 3-hourly resolutions from the Global Data Assimilation System (GDAS) to calculate backward trajectories (see Section 2.4 for details).

Statistical analyses primarily involved linear correlations and regressions, with the coefficient of determination (R^2) used to quantify the variance explained by each variable. In addition, we used composite analysis to reveal relationships between variables. For example, to identify general patterns in backward trajectories associated with *d*-excess exceeding 30‰, all the days with such high *d*-excess values were compiled into a collection. A composite map of trajectories from this collection was then constructed to reveal typical pathways under these conditions.

2.3 Theoretical framework for understanding isotope compositions and humidity

In addition to complex atmospheric circulation models, the evolution of vapor isotope compositions during different moistening and dehydration processes can be predicted through a compilation of atmospheric processes such as condensation, mixing, and raindrop evaporation (Worden et al., 2007; Noone, 2012; Galewsky et al., 2016). These processes shape distinct pathways of isotopic evolution in relation to atmospheric humidity.

The Rayleigh distillation model describes the progressive condensation of water vapor (Dansgaard, 1964). The isotopic composition of the remaining vapor, denoted as δ, can be expressed as $\delta = (1 + \delta_0)(q/q_0)^{\alpha-1} - 1$, where q is the specific humidity, and α is the fractionation factor. A subscript of 0 refers to the initial condition of the air mass. Raindrop evaporation introduces further complexity. As raindrops form at higher altitudes where vapor is depleted in heavy isotopes, their partial evaporation affects the surrounding vapor, leading to isotope values lower than those predicted by Rayleigh models (Worden et al., 2007; Risi et al., 2008a). This effect gives rise to “super-Rayleigh” trajectories, characterized by an inflated effective

fractionation factor (α_e), defined as $\alpha_e = (1 + \phi)\alpha$, where ϕ quantifies deviations from equilibrium. Notably, Worden et al. (2007) and Noone (2012) have given different equations for such deviations, and this study aligns with the formulations by Noone (2012).

Air mass mixing also influences humidity and isotopic compositions. When a dry air mass mixes with a moist mass, the specific humidity of the mixed air can be described as $q = f_{dry}q_{dry} + f_{moist}q_{moist}$, where f represents the fraction of each air mass, with $f_{dry} + f_{moist} = 1$. Isotopic compositions are similarly derived by solving mass balance equations for the light and heavy isotopes, resulting in a hyperbolic relationship between δ and q. In other words, $\delta \times q$ and q should have a linear relationship in the mixing process (Fiorella et al., 2018). The intercept of the regression between δ and $1/q$ or the slope between $\delta \times q$ and q provides an estimate of the moist end member's isotopic composition (Keeling, 1958).

Assuming a surface temperature of 25 °C and a relative humidity of 85%, we utilize the evaporation model of Craig and Gordon (1965) to determine the isotopic composition of ocean evaporation. This results in $\delta^{18}O$ = −11.5‰, $\delta^{2}H$ = −81.4‰, and *d*-excess = 10.6‰. These values serve as the wet end member for modeling the moistening process through mixing with ocean evaporation. For the dry end member, we consider a dehydrated air mass from the Rayleigh curve at q = 0.5 g/kg, $\delta^{18}O$ = −60.3‰, and $\delta^{2}H$ = −418.0‰ (Fig. S2). The dehydration process via condensation is initiated at a relative humidity of 80% on the mixing line. Similarly, "super-Rayleigh" distillation involving partial rain evaporation also begins from this starting point. We explore two "super-Rayleigh" scenarios: Rain_evap_A assumes 2% rain evaporation, whereas Rain_evap_B assumes 5% rain evaporation, which is based on equations from Noone (2012). Additionally, we consider the influence of evapotranspiration over South Asia and the TP on atmospheric humidity and vapor isotope compositions over the SETP. Quantifying the isotopic compositions of land surface evapotranspiration is challenging. Given that precipitation $\delta^{18}O$ over South Asia generally ranges from −1.0‰ to −5.0‰ (Bowen and Wilkinson, 2002; Terzer-Wassmuth et al., 2021) and that transpiration constitutes two-thirds or more of evapotranspiration (Good et al., 2015; Cao et al., 2022; Han et al., 2022), we assume a $\delta^{18}O$ value of −5.0‰ as an upper bound for land surface evapotranspiration. Similarly, we assume a *d*-excess of 15.0‰ for this wet end member.

2.4 Backward trajectory and moisture source diagnostic

To investigate air mass transport and diagnose moisture sources and pathways toward SETP, we calculated backward trajectories using the Hybrid Single-Particle Lagrangian Integrated Trajectory model (HYSPLIT) (Stein et al., 2015). Trajectory calculations were driven by nested ERA5 (within the domain of 0–50°N and 40–120°E) and GDAS (globally but outside of the ERA5 domain) data to achieve higher resolution in the major potential source regions. In addition, the vertical motion was driven by the model vertical velocity. Air parcels were released from 5 locations: the study site and points displaced 0.2° in each cardinal direction. These releases occurred at 7 different vertical levels: 10, 50, 100, 200, 300, 400, and 500 m above ground level. For each day during the sampling campaign, trajectories were initiated every 3 hours to calculate 10-day

backward trajectories, resulting in 280 trajectories per day. Geographical and meteorological variables, including location, pressure, temperature, specific humidity, rainfall amount, boundary layer height, and terrain height along the trajectories, were stored at hourly intervals.

To quantify moisture contributions along trajectories to SETP's humidity, we applied the Lagrangian moisture source diagnostic method developed by Sodemann et al. (2008). This method uses mass balance principles along trajectories, interpreting increases in specific humidity (forward in time) as moisture uptake and decreases as moisture loss due to precipitation occurs. It also accounts for the reduced contribution of earlier moisture uptake due to precipitation en route. We previously adapted this method to identify moisture sources for precipitation in subregions of South Asia and East Asia (Cai et al., 2018; Cai and Tian, 2020). A more detailed description of the moisture source diagnostic method can be found in Sodemann (2025).

In this framework, the moisture source can be attributed into four categories: contributions within an extended boundary layer over 1) land and 2) ocean, 3) contributions from above the extended boundary layer, and 4) remaining unattributed sources. Following Sodemann et al. (2008), the extended boundary layer was parameterized as 1.5 times the boundary layer height. The diagnostic results indicated that approximately 7.0% of the moisture arriving at the SETP remained unattributed, confirming that 10-day trajectories are sufficient to diagnose most moisture sources. Overall, the fractions of within-boundary-layer contributions are 60.2% over land and 5.0% over ocean, with an additional 27.8% originating from above the extended boundary layer. To investigate the relationship between vapor *d*-excess and relative humidity (RH) at moisture sources, we diagnosed a set of RH-related variables. The RH^{source} is the weighted-mean RH at locations where within-boundary-layer moisture uptakes occur by weighting the individual within-boundary-layer moisture contributions. The RH^{source_land} and RH^{source_ocean} are similar to the RH^{source} but only apply to within-boundary-layer moisture uptakes over land and ocean, respectively. The $RH_{SST}^{source\_ocean}$ is the weighted-mean RH_{SST} at locations where within-boundary-layer moisture uptakes occur over ocean by weighting the individual within-boundary-layer moisture contributions.

Additionally, this study emphasizes the contributions of air parcels themselves to the humidity of the SETP. This variable captures the history of the moisture and indicates how much moisture within each air parcel finally reaches the SETP. The moisture contribution of an air parcel to the SETP's humidity is a measure of the importance of upstream air. We calculated weighted-mean upstream variables using the moisture contribution of the air parcel along trajectories as the weight. We also applied K-means clustering to group trajectories, helping to identify major transport pathways. When calculating the mean trajectory for each cluster and the meteorological variables along each mean trajectory, the moisture contribution of the air parcel is also considered as the weight to calculate the weighted means.

3 Results

3.1 General characteristics of vapor δ18O, d-excess, and local meteorological variables

Consistent with Yao et al. (2013), we defined June−September (JJAS) as the summer monsoon season. In contrast, November−April (Nov-Apr) was designated as the non-monsoon season, with May and October considered transition periods between the two seasons. In general, the $\delta^{18}O$ values are relatively low during the summer monsoon season and relatively high during the non-monsoon season (Fig. 1a). The mean $\delta^{18}O$ values are −18.4‰ for the non-monsoon season, −23.3‰ for the summer monsoon season, −16.9‰ for May, and −22.8‰ for October. $\delta^{18}O$ shows a dramatic decrease at the onset of the summer monsoon. Conversely, from the end of the summer monsoon season to spring and early summer, the $\delta^{18}O$ values gradually increase. Although the amount effect significantly influences this region, the seasonal variation in $\delta^{18}O$ does not strictly align with local precipitation patterns. For example, although local precipitation clearly ceases after the summer monsoon (Fig. 1e), $\delta^{18}O$ remains at relatively low levels. This behavior is consistent with precipitation $\delta^{18}O$ values in the SETP, northeast India, and Bangladesh (Yao et al., 2013; Yang et al., 2017; Cai and Tian, 2020).

Although *d*-excess values are also lower during the summer monsoon season and higher during non-monsoon periods, the timing of seasonal transitions differs from that of $\delta^{18}O$ (Fig. 1b). The mean *d*-excess values are 18.3‰ for the non-monsoon season, 11.9‰ for the summer monsoon season, 13.7‰ for May, and 14.9‰ for October. The highest *d*-excess values generally occur during the winter months, when the air temperature and relative humidity (RH) are at their lowest levels (Fig. 1c and 1d). Furthermore, *d*-excess starts to decrease in spring, earlier than the sharp drop in $\delta^{18}O$ at the onset of the summer monsoon.

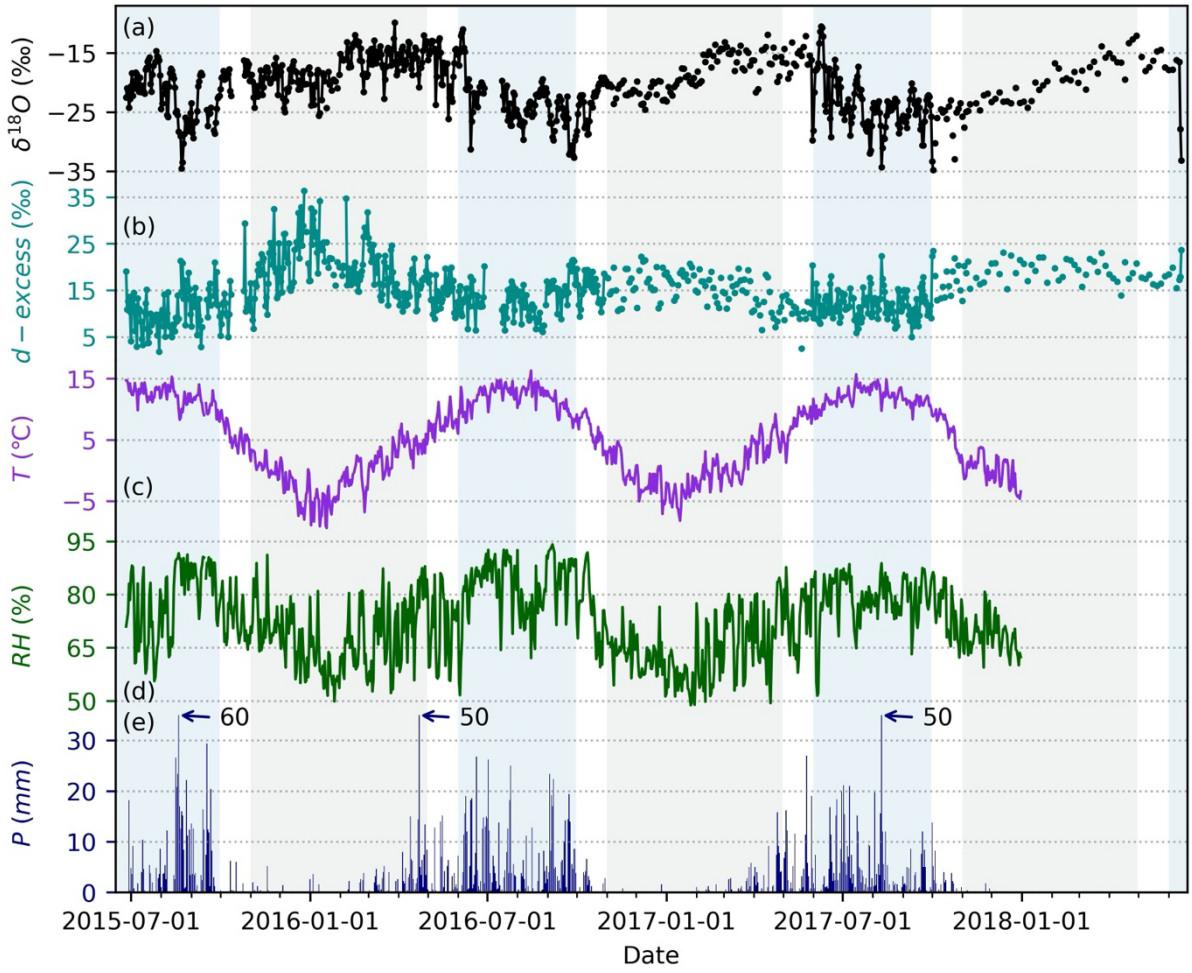

Figure 1: Time series of observed vapor $\delta^{18}O$, *d*-excess, and daily local meteorological variables from 2015–2018: (a) $\delta^{18}O$, (b) *d*-excess, (c) air temperature, (d) relative humidity (RH), and (e) precipitation amount. The light blue shading highlights the summer monsoon season, whereas the light steel blue shading indicates the non-monsoon season.

The linear relationship between paired $\delta^{18}O$ and $\delta^{2}H$ values (Fig. 2), along with their position relative to the global meteoric water line (GMWL, $\delta^{2}H = 8\delta^{18}O + 10$) (Craig, 1961), provides additional insights into isotopic fractionation processes (Putman et al., 2019). The local vapor line (LVL), estimated from all the $\delta^{2}H$ and $\delta^{18}O$ data points, is $\delta^{2}H = 7.96\delta^{18}O + 14.04$ (R^2 = 0.98). This LVL plots above but approximately parallel to the GMWL. This relatively high intercept of the LVL reflects the continental location of the site and additional kinetic fractionation after ocean evaporation. The $\delta^{2}H$–$\delta^{18}O$ relationship also varies seasonally. During the non-monsoon season, the LVL is $\delta^{2}H = 7.58\delta^{18}O + 10.61$ ($R^2 = 0.96$), whereas during the summer monsoon season, it shifts to $\delta^{2}H = 7.53\delta^{18}O + 0.91$ ($R^2 = 0.99$). Non-monsoon data primarily plot above both the GMWL and the overall LVL. Conversely, most monsoon season isotope data fall below the overall LVL, although the lowest δ value points during this period are positioned above the overall LVL, suggesting additional kinetic fractionation, such as rain evaporation (He et al., 2024). The vapor isotopes for May resemble those of the non-monsoon season but align more closely with both the GMWL and the LVL, whereas the data for October exhibit behaviors similar to those of the monsoon season observations.

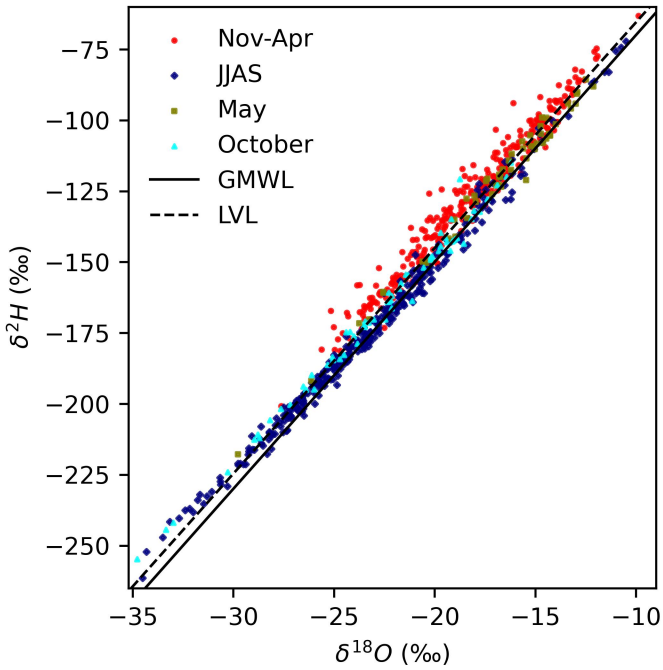

Figure 2: Relationship between vapor δ²H and δ¹⁸O. The data are presented for different seasons: non-monsoon (Nov-Apr) as red dots, summer monsoon (JJAS) as navy diamonds, May as olive squares, and October as cyan triangles. The solid line indicates the global meteoric water line (GMWL). The dashed line indicates the local vapor line (LVL) estimated from all the δ²H and δ¹⁸O data points.

The relationships between $\delta^{18}O$ and specific humidity (q) further indicate distinct seasonal patterns in moisture dynamics (Fig. 3a). Owing to the lack of avilability of local meteorological data for 2018, our analyses focused on data collected before 2018. During the non-monsoon season, particularly in the winter months, most data points are positioned above the Rayleigh distillation line but below a mixing line that represents an upper bound of hypothetical evapotranspiration over South Asia. This suggests a mixture of dry end members and moist end members. In contrast, during the summer monsoon season, data predominantly fall below the Rayleigh line, which is influenced by "super-Rayleigh" processes linked to rain evaporation.

Further insights come from examining $\delta \times q$ versus q relationships, which highlight seasonal contrasts in moisture source signatures (Fig. S3). For the non-monsoon season, a simple estimation through the linear regression between $\delta \times q$ and q suggests a moist end member with a $\delta^{18}O$ of −13.9‰ ± 0.6‰. The weighted annual mean precipitation $\delta^{18}O$ at our site was approximately −14.5‰ (Yao et al., 2013). However, during the monsoon season, the overall estimation of $\delta^{18}O$ for the moist end member through the linear regression between $\delta \times q$ and q is significantly lower at −30.9‰ ± 1.8‰, indicating that an additional moisture source from rain evaporation is more depleted in heavy isotopes. These results align with the distribution of $\delta^{18}O$-q data below the Rayleigh line during the summer monsoon season (Fig. 3a), underscoring the influence of different moisture sources and processes across seasons.

The relationships between d-excess and q also reflect seasonal contrasts in moisture dynamics (Fig. 3b). During the non-monsoon season months, a negative correlation is observed, where a lower q corresponds to a higher d-excess value (Figs. 1 and 3b). This relationship is particularly pronounced under dry and cold conditions. In contrast, during the summer monsoon

season, no clear relationship between *d*-excess and *q* is apparent, with *d*-excess showing considerable variability of approximately 20‰ at any given *q*. These findings suggest that *d*-excess is less predictable than $\delta^{18}O$ when using *q*, except at low humidity levels.

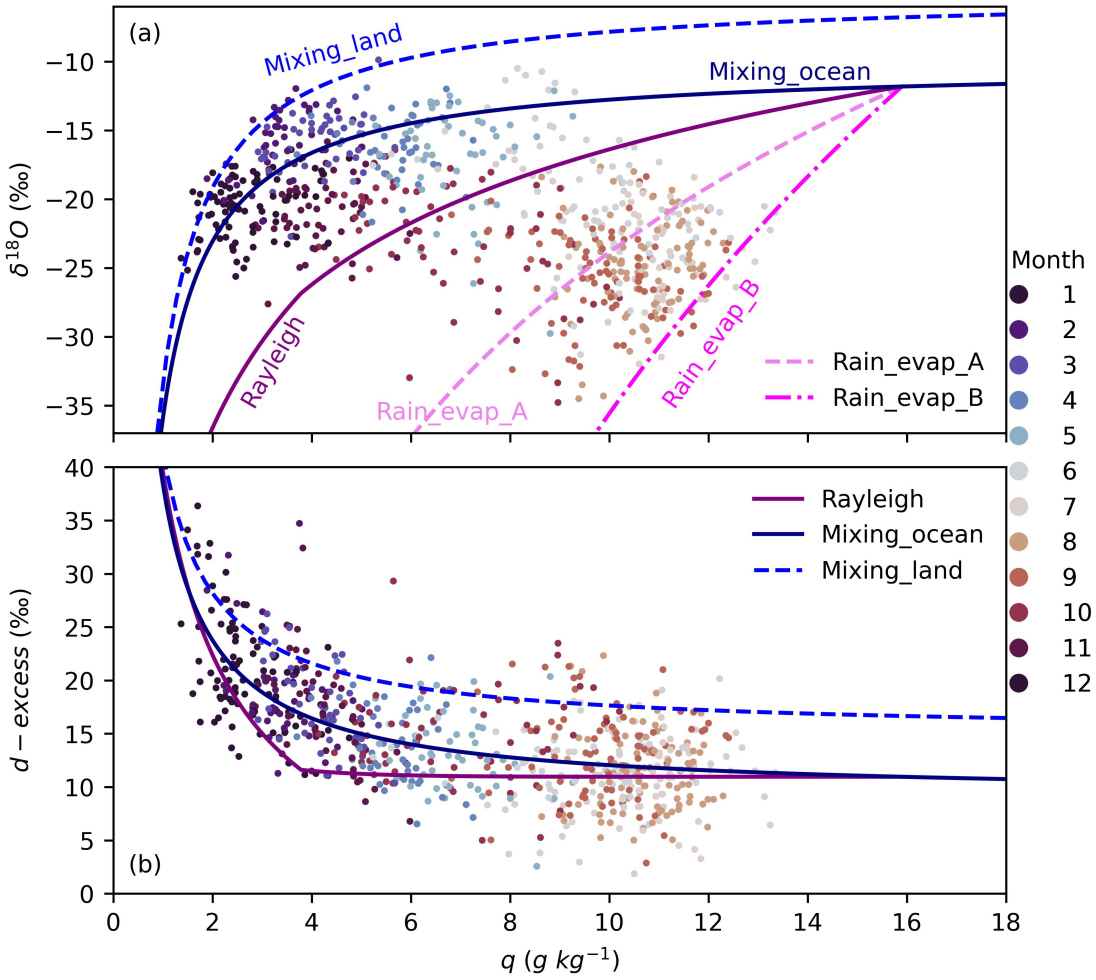

Figure 3: Relationships between vapor isotopes ($\delta^{18}O$ and *d*-excess) and specific humidity (*q*) from 2015–2017. (a) Scatter plot of $\delta^{18}O$ against *q*. (b) Scatter plot of *d*-excess against *q*. Each data point is color-coded by month. The reference lines correspond to those in Fig. S2; their interpretations are detailed in Fig. S2 and Section 2.3. Note that only data before 2018 are shown (see text for details).

3.2 Seasonal variability in moisture sources and transport pathways

To understand the drivers behind the seasonal variations in moisture dynamics, we analyzed the moisture sources and transport pathways during different seasons (Fig. 4). Our focus was on the contribution of moisture from historical air masses (last 10 days) to humidity at SETP.

During the non-monsoon season (Fig. 4a), moisture is mainly transported via two main pathways: one originating from the west of SETP, carried by the westerlies (clusters Nov-Apr2 and Nov-Apr3), and the other from the south, such as the BOB (cluster Nov-Apr1). The quantitative contributions are 84.8% from the southern pathway and 15.2% from the western branches combined. Interestingly, when considering only trajectories without accounting for moisture contributions, all three clusters appear to originate from the west or southwest of the SETP (Fig. S4). This discrepancy highlights the importance of

distinguishing between pure air mass transport and actual moisture sources when trajectory data are interpreted.

In contrast, during the summer monsoon season (Fig. 4b), moisture transport is predominantly from the south of the SETP, which is driven by the summer monsoon. The pathways observed in May (Fig. 4c) represent a transition from the non-monsoon season (Fig. 4a) toward the dominant southerly transport observed during the summer monsoon (Fig. 4b). In comparison, the moisture sources and transport pathways exhibit a slight eastward shift during October compared with those during the summer monsoon season (Figs. 4d and S4d).

Another notable aspect of the moisture source distributions is the dominant contribution from proximal terrestrial regions, particularly those to the south of the SETP (Fig. 4). For example, the 1% contour representing moisture contributions from air parcels over each 1°×1° grid box does not extend or barely extends into oceanic regions during any of the four seasons. This finding indicates that surface evaporation from oceanic regions such as the BOB and AS contributes minimally. Quantitatively, the within-boundary-layer contributions from oceanic regions are determined to be 2.5%, 9.1%, 4.6%, and 2.0% for non-monsoon, summer monsoon, May, and October, respectively. Most of the moisture originating over these oceanic regions is lost through precipitation before reaching the SETP, and what remains is replenished by evapotranspiration during transport over land. This finding raises an important question: do the vapor isotopes measured at the SETP still reflect the meteorological conditions at their oceanic sources?

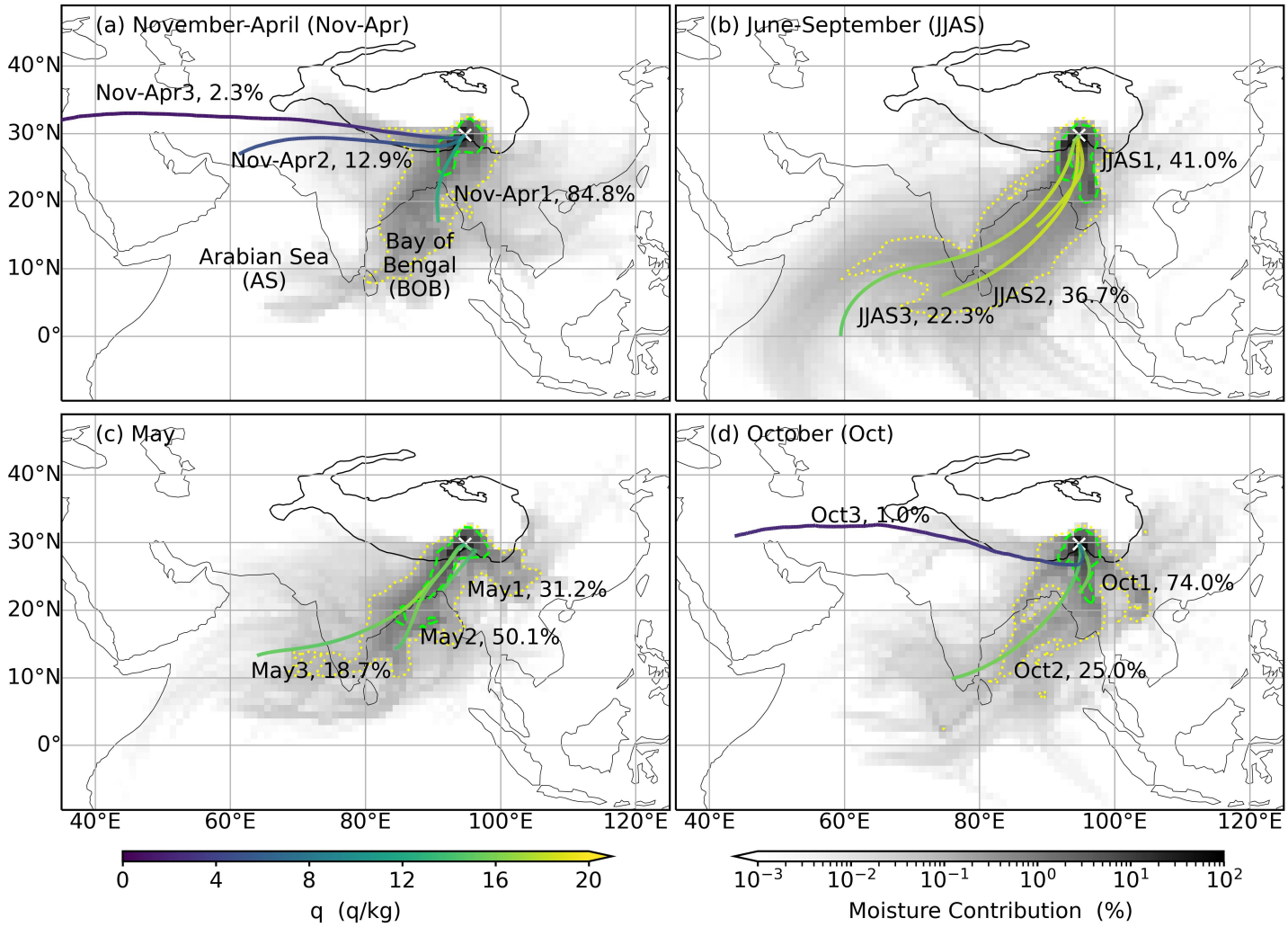

Figure 4: Moisture sources and transport pathways during different seasons from 2015–2017. (a) Spatial distribution of relative contributions of moisture from all air parcels over each 1°×1° box (shading) to humidity at the SETP station, along with specific humidity (*q*) along mean trajectories (weighted by moisture contributions) for the non-monsoon season of November–April (Nov-Apr). (b-d) Same as (a), but for the monsoon season of June–September (JJAS, b), May (c), and October (d), respectively. The dotted yellow and dashed green contours indicate the moisture contributions at 0.1% and 1%, respectively. The yellow crosses indicate the location of the SETP station. The black solid lines denote the Tibetan Plateau with an altitude contour at 3000 m.

3.3 Role of ocean surface evaporation conditions at seasonal and intraseasonal time scales

Relationships between *d*-excess and ocean surface evaporation conditions, such as RH_{SST} and SST, were examined using data from 2015–2017 (Figs. 5a and Fig. S5a). The results indeed show negative correlations between *d*-excess and RH_{SST} over the northern Indian Ocean, particularly in the northern parts of the AS and BOB (Fig. 5a). Specifically, the regression slopes for this relationship across the northern Indian Ocean vary from higher than –0.1‰ $\%^{-1}$ to values below –0.6‰ $\%^{-1}$.

Focusing on specific regions, the northern BOB (10–22°N and 80–99°E) and the eastern AS (7–20°N and 65–78°E; Fig. 5a) presented regression slopes within the range of –0.3‰ $\%^{-1}$ to –0.6‰ $\%^{-1}$ previously reported (Uemura et al., 2008; Benetti et al., 2014; Liu et al., 2014; Bonne et al., 2019). For example, the regional average RH_{SST} in the eastern AS shows an overall regression slope of –0.49‰ $\%^{-1}$ ($r = -0.52$ and $p < 0.01$) (Fig. 6a), whereas the northern BOB has a slope of –0.52‰ $\%^{-1}$ ($r = -0.55$ and $p < 0.01$) (Fig. 6b). However, the clustering of data points by season (Fig. 6) suggests that the apparent negative

correlations might primarily stem from opposing seasonal trends. Similarly, apparent negative correlations between *d*-excess and SST also emerge over the northern Indian Ocean (Fig. S5a). However, both theoretical predictions (Merlivat and Jouzel, 1979) and in situ observations above the ocean surface (Liu et al., 2014; Bonne et al., 2019) reveal a positive correlation between *d*-excess and SST. These discrepancies lead us to speculate that the overall correlations between the SETP vapor *d*-excess and surface evaporation conditions over the northern Indian Ocean are likely driven by seasonal variability.

The relationship between *d*-excess and RH_{SST} was further analyzed by distinguishing between the summer monsoon and non-monsoon seasons. During the summer monsoon season, the negative correlation diminishes significantly, with correlation coefficients dropping below 0.3 (Fig. 5b). In contrast, significant correlations are present during the non-monsoon season (Fig. 5c), potentially due to intraseasonal variations where *d*-excess peaks in winter and decreases at the beginning and end of the non-monsoon season (Fig. 1b), possibly accompanied by opposing RH_{SST} trends. Although the correlation is significant during the non-monsoon season, the explained variance in *d*-excess remains low, at a maximum of 10%–16% over the northern BOB. Similarly, correlations with SST over the northern Indian Ocean also become negligible when seasons are considered separately (Fig. S5). To account for transport time, we examined correlations between *d*-excess and RH_{SST} from 1–11 days prior to the *d*-excess observation dates during the summer monsoon (Fig. S6) and non-monsoon seasons (Fig. S7), respectively. The results are consistent with those shown in Fig. 5, indicating that considering these lagged timeframes does not enhance the correlation between *d*-excess and RH_{SST}.

To further explore the relationships between *d*-excess and RH over moisture source regions, we analyzed the correlations between *d*-excess and the RH-related variables for all observations from 2015–2017 and during the four seasons (Table 1). Overall, *d*-excess is significantly negatively correlated with these RH-related variables at moisture sources at the annual scale, whereas correlations during specific seasons weaken to very low levels. The strongest correlation is between *d*-excess and RH^{source} from 2015–2017 ($r = -0.48$, $p < 0.01$). Notably, correlations with $RH_{SST}^{source\_ocean}$ are weak overall (Table 1). In summary, vapor *d*-excess at the SETP is less likely a conservative tracer of surface evaporation conditions (neither RH_{SST} nor SST) over the northern Indian Ocean. Therefore, interpreting *d*-excess in meteoric water or paleo archives from the TP as a proxy for Indian Ocean evaporation conditions should be approached with caution.

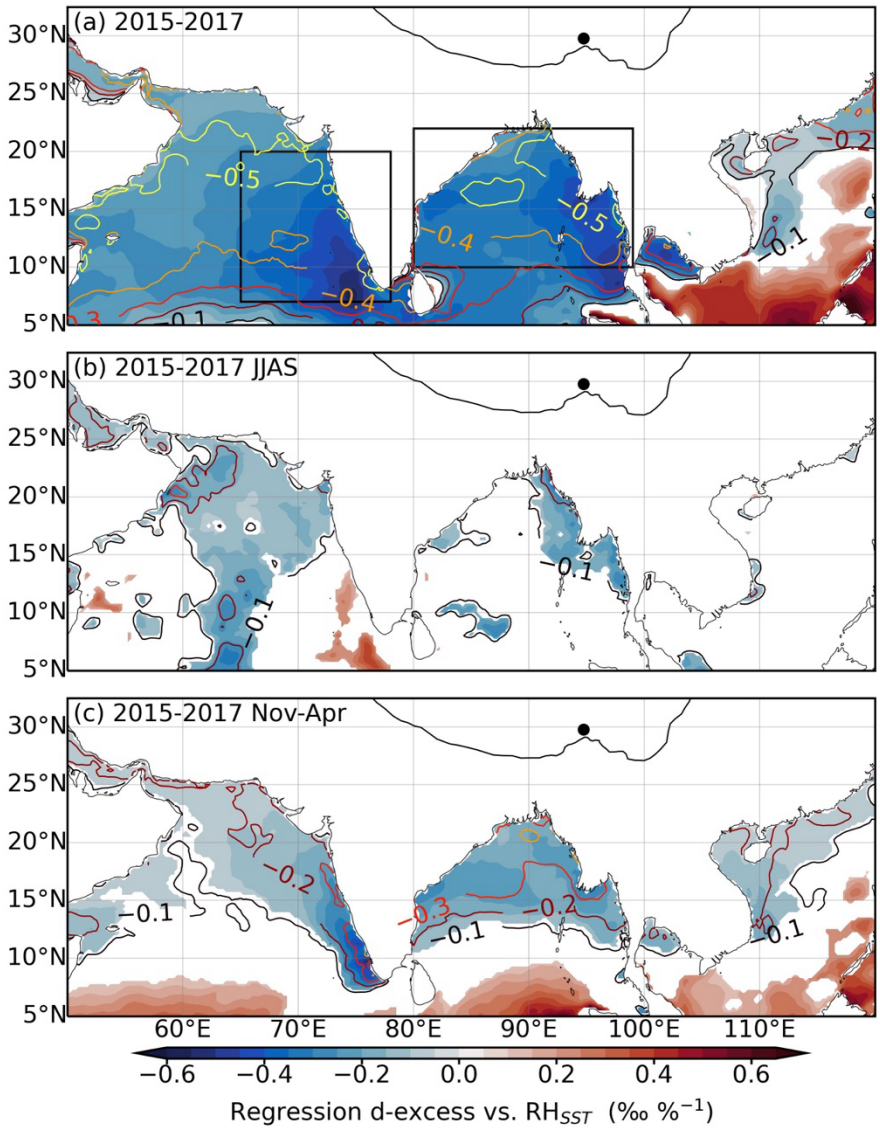

Figure 5: Relationships between vapor *d*-excess and relative humidity scaled to sea surface temperature (RH$_{SST}$). (a) Regression of *d*-excess against RH$_{SST}$ (shading and only values significant at the 95% significance level are shown) and correlation coefficients between them (contours at an interval of 0.1 and only negative correlations are shown) for all the data from 2015–2017. (b) and (c) are the same as (a) but only for the data within the summer monsoon season (JJAS) or the non-monsoon season (Nov-Apr), respectively. The black dots indicate the location of the SETP station. The black solid lines denote the Tibetan Plateau with an altitude contour at 3000 m.

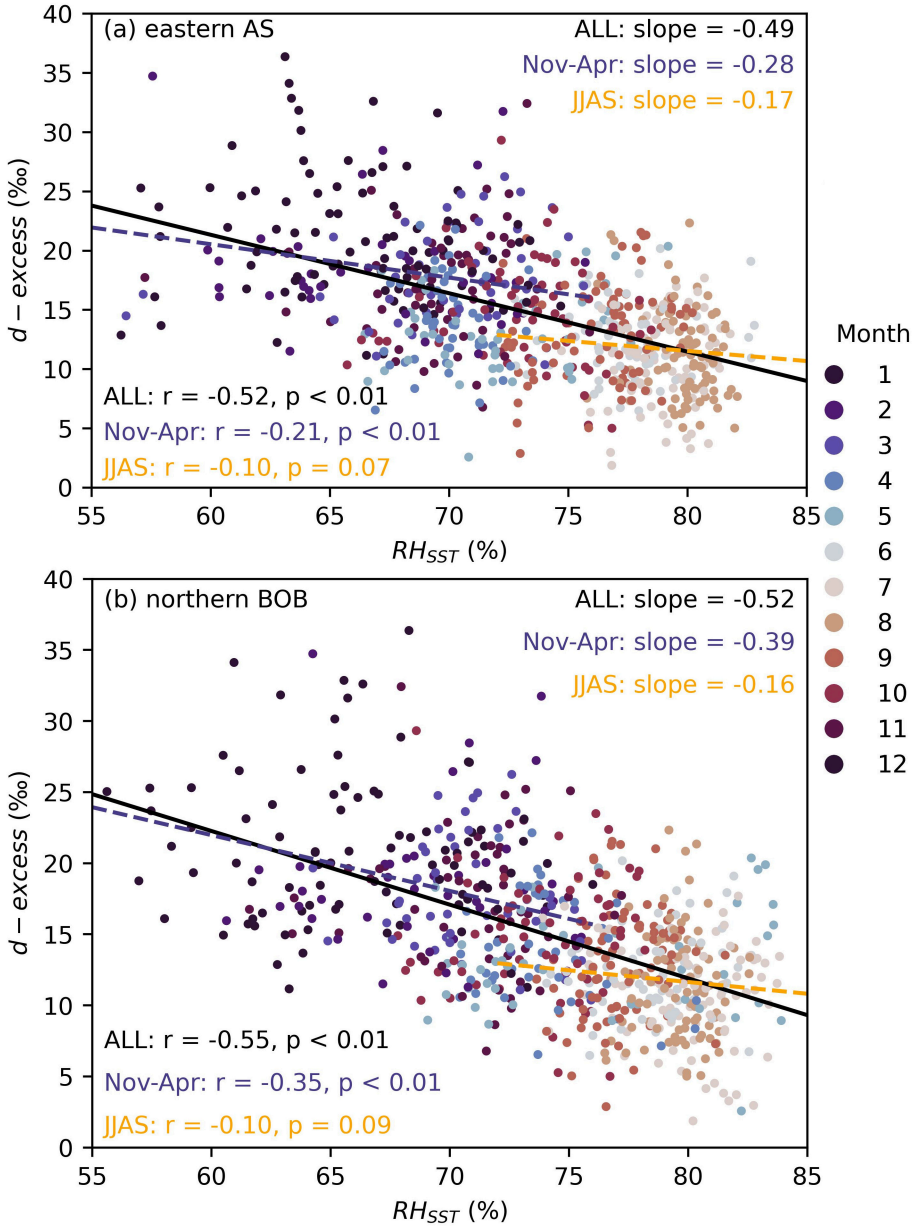

Figure 6: Relationships between SETP vapor *d*-excess and relative humidity normalized to sea surface temperature (RH_{SST}) averaged over (a) the eastern Arabian Sea (7–20°N and 65–78°E) and (b) the Bay of Bengal (10–22°N and 80–99°E) from 2015–2017. Each data point is color-coded by month. The solid black lines indicate the linear regression between all the data points. The dashed orange lines indicate linear regression for data during the non-monsoon season (Nov-Apr), and the dashed dark blue lines indicate data during the summer monsoon (JJAS). The slopes (‰ $\%^{-1}$), r values, and p values for the three data groups are also shown.

Table 1: Correlation coefficients between *d-excess* and the RH-related variables for different seasons from 2015–2017. Values with significance levels exceeding 99%, between 99% and 95%, 95% and 90%, are in bold italics, bold, and italics, respectively.

	2015-2017 All	Nov-Apr	JJAS	May	Oct
RH^{source}	***−0.48***	***−0.24***	0.08	*0.27*	*0.23*
RH^{source_land}	***−0.17***	0.01	0.02	0.13	0.16
RH^{source_ocean}	***−0.23***	***−0.30***	0.02	0.04	0.01

$RH_{SST}^{source\_ocean}$	***−0.37***	**−0.17**	***−0.30***	**−0.35**	−0.16

3.4 Role of dry and cold air intrusion during the non-monsoon season

Both theoretical predictions from the Rayleigh model and observations during the non-monsoon season suggest that *d*-excess increases as *q* decreases when *q* reaches extremely low values (Fig. 3b). In addition, the results for both air mass transport and moisture transport reveal the significant role of the westerlies (Figs. S4a and 4a). Based on this evidence, we propose that during the non-monsoon season, vapor isotopes are influenced by the mixing of cold and dry air transported by westerlies from higher altitudes with surface vapor. Furthermore, surface vapor influenced by recycled moisture from terrestrial evapotranspiration would further elevates *d*-excess at a given *q* (Fig. 3b).

We performed a composite analysis of moisture sources and transport pathways for the highest (higher than 30‰, and n = 10) and lowest (lower than 10‰, and n = 8) *d*-excess observations during the non-monsoon season (Fig. 7). High *d*-excess values are associated primarily with moisture transported by westerlies from regions west or southwest of the SETP, such as over the TP and northern India. In addition, backward trajectories for these cases show air masses characterized by extremely low *q* values, reaching below 2 g kg^{-1} along the mean trajectories (weighted by moisture contribution) across the TP (Fig. 7a). Conversely, for low *d*-excess cases, the moisture transport pathways shift toward more humid regions south of the SETP, including northeast India, Bangladesh, and the BOB (Fig. 7b). This contrasting moisture transport pattern between high and low *d*-excess cases aligns with our hypothesis that high *d*-excess values are associated with dry and cold air transported by westerlies.

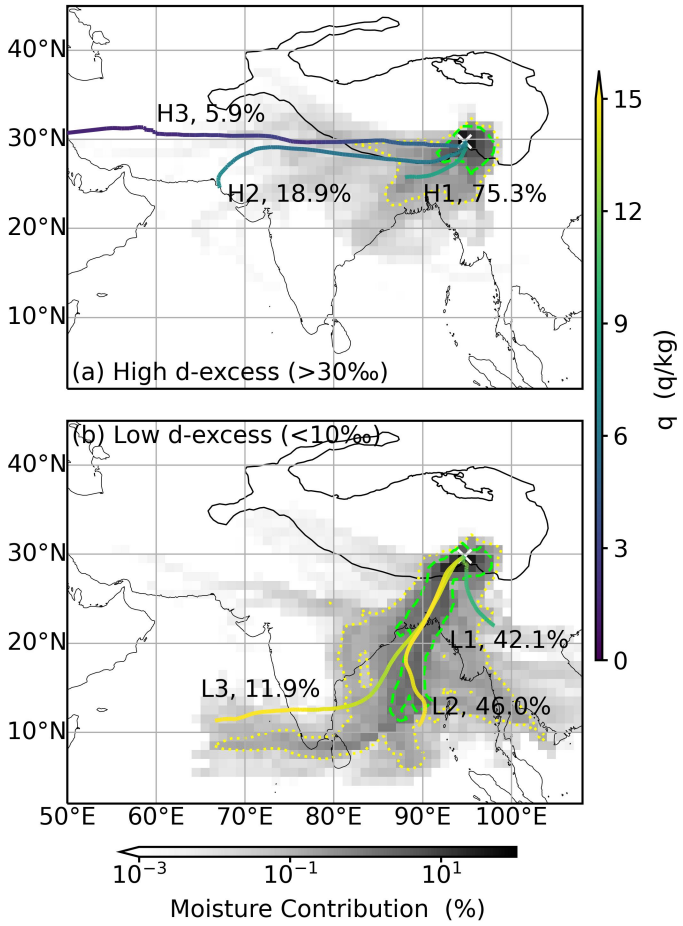

Figure 7: Composite of moisture sources and transport pathways for high and low *d*-excess days during the non-monsoon season from November–April. (a) Spatial distribution of the relative contribution of moisture from all air parcels over each 1°×1° box (shading) to humidity at the SETP station, along with specific humidity (*q*) along mean trajectories (weighted by moisture contributions) for *d*-excess values higher than 30‰ during the non-monsoon season (n = 10). (b) Same as (a) but for *d*-excess values lower than 10‰ (n = 8). The yellow crosses indicate the location of the SETP station. The black solid lines denote the Tibetan Plateau with an altitude contour at 3000 m.

The influence of cold and dry air intrusions was further investigated through an analysis of relationships involving *d*-excess, local *q*, weighted-mean upstream *q*, weighted-mean upstream air temperature, and weighted-mean upstream air altitude (Fig. 8). The upstream variables represent weighted averages along the 10-day backward trajectory, where the weights correspond to the moisture contribution at each time step (Section 2.4). The non-monsoon season *d*-excess shows robust negative correlations with both local *q* ($r = -0.65$, $p < 0.01$; Fig. 8a) and upstream *q* ($r = -0.48$, $p < 0.01$). Furthermore, local *q* is strongly linked with upstream *q* ($r = 0.83$, $p < 0.01$; Fig. 8b), which is associated with air masses characterized by low temperatures and high altitudes (Fig. 8c and d). Additionally, the properties of the upstream air could also impact $\delta^{18}O$. Indeed, the $\delta^{18}O$ values during high *d*-excess cases are lower than those during low *d*-excess cases (at a significance level of 95.3%). The overall correlation coefficient between $\delta^{18}O$ and *d*-excess during the non-monsoon season is −0.29 ($p < 0.01$). Notably, the correlations between $\delta^{18}O$ and *q* are weaker than those observed for *d*-excess, with local *q* showing $r = 0.42$ ($p < 0.01$) and upstream *q* showing $r = 0.41$ ($p < 0.01$). The relationship between non-monsoon season $\delta^{18}O$ and humidity is expressed mainly as the relationship between $\delta \times q$ and q ($r = 0.82$ for local *q* and $r = 0.80$ for upstream *q*). Spatial correlations between vapor

isotopes ($\delta^{18}O$ and *d*-excess) and 2-meter air temperature as well as humidity measured by the 2-meter dew point temperature also support these findings (Fig. S8). Significant negative correlations between *d*-excess and dew point temperatures exist over the Southeast TP, northeast India, and northern Bangladesh. In contrast, $\delta^{18}O$ shows significant positive correlations with air temperature over the Indian subcontinent and northwestern Southeast Asia.

As shown in Fig. 3b, extremely high *d*-excess values are predicted at very low *q* levels. Previous studies have shown that as *q* approaches zero, vapor *d*-excess can approach 7000‰ following the Rayleigh distillation trajectory (Bony et al., 2008), a behavior inherent to the definition of *d*-excess (Dütsch et al., 2017). High *d*-excess values have also been observed in low-humidity environments, such as polar regions (Bonne et al., 2014; Steen-Larsen et al., 2017) and high altitudes (Webster and Heymsfield, 2003; Samuels‐Crow et al., 2014; Sodemann et al., 2017). Therefore, we infer that the increasing trend of *d*-excess with decreasing local *q*, upstream *q,* and regional dew point temperature is due to enhanced mixing with dry and cold subsiding air transported by westerlies from high altitudes. The relationships between upstream *q* and upstream air temperature as well as altitude further support this inference, indicating that low-humidity conditions are associated with the presence of subsiding dry and cold air from high altitudes (Fig. 8c and d). Therefore, vapor *d*-excess during the non-monsoon season not only provides insights into specific humidity levels but also reveals the source of humidity.

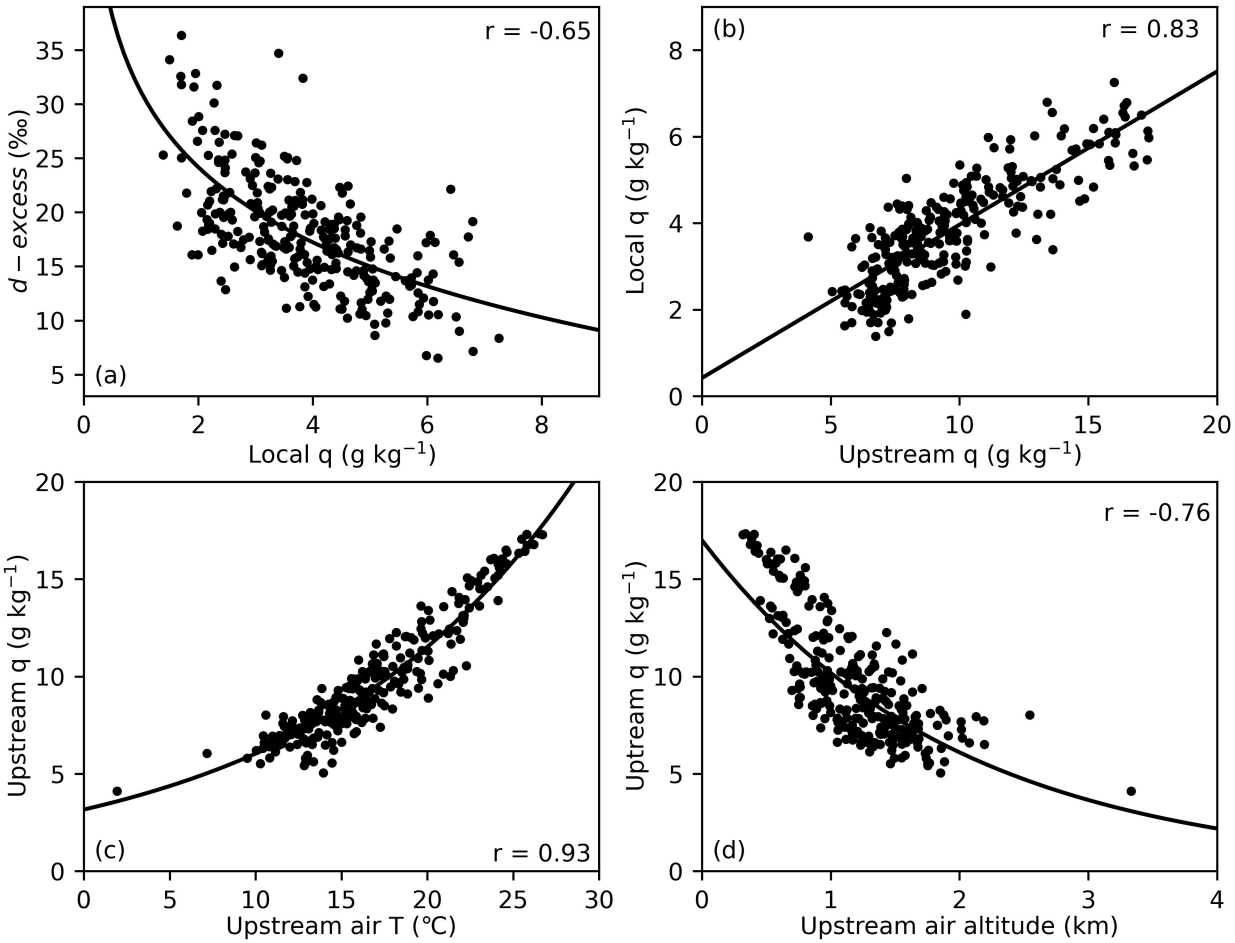

Figure 8: Relationships among vapor *d*-excess, local specific humidity (*q*), weighted-mean upstream *q*, weighted-mean upstream air temperature (T), and weighted-mean upstream air altitude during the non-monsoon season from November–April. (a) Scatter plot of *d*-excess against local *q*. (b) Scatter plot of local *q* against upstream weighted-mean

***q*. (c) Scatter plot of upstream *q* against upstream air T. (d) Scatter plot of upstream *q* against upstream air altitude. All the upstream variables are mean values along backward trajectories weighted by the moisture contribution of air parcels. The solid curves indicate the log (a, c, and d) or linear (b) regression between the respective variables, with the correlation coefficients indicated by the numbers.**

3.5 Role of precipitation–vapor interaction during the summer monsoon season

In contrast to the significant dependence of *d*-excess on *q* during the non-monsoon season, no correlation is detected ($r = 0.04$, $p = 0.51$) during the summer monsoon season. The behavior of $\delta^{18}O$ also differs between the two seasons (Fig. 3). During the summer monsoon season, $\delta^{18}O$-*q* plots below the Rayleigh curve, indicating that the vapor has experienced precipitation–vapor interactions through rain evaporation (Fig. 3a). Partial rain evaporation in an unsaturated atmospheric environment leads to kinetic fractionation, which decreases *d*-excess values in raindrops while increasing *d*-excess values in the surrounding vapor (Risi et al., 2008b). This effect of precipitation–vapor interactions on vapor isotopes has been suggested as a primary mechanism driving the amount effect in tropical regions (Risi et al., 2008a; Kurita et al., 2011; Galewsky et al., 2016; Bowen et al., 2019). Therefore, we hypothesize that vapor isotopes during the summer monsoon season at the SETP station are influenced by the extent of precipitation–vapor interactions.

The first evidence supporting this hypothesis is the significant correlation between $\delta^{18}O$ and *d*-excess during the summer monsoon season ($r = -0.55$, $p < 0.01$; Fig. 9a). In addition, $\delta^{18}O$ and *d*-excess tend toward weak correlations at high $\delta^{18}O$ values but stronger correlations when $\delta^{18}O$ values are low (Figs. 9a and S9). To explore this further, we categorized days with daily precipitation of at least 2 mm as “rainy days” and those with daily precipitation of less than 2 mm as “non-rainy days”. This distinction is based on the premise that precipitation–vapor interactions cannot occur in the absence of precipitation. The analysis reveals that the $\delta^{18}O$ values during rainy days are significantly lower than those during non-rainy days, whereas the *d*-excess values show the opposite trend ($p < 0.01$ for both $\delta^{18}O$ and *d*-excess; Figs. 9b and 9c). Furthermore, the correlation between $\delta^{18}O$ and *d*-excess becomes stronger on rainy days ($r = -0.69$, $p < 0.01$), although a weaker negative correlation persists even on non-rainy days ($r = -0.40$, $p < 0.01$). Even when a stricter threshold of 0 mm is applied for non-rainy days, the negative correlation between $\delta^{18}O$ and *d*-excess remains significant ($r = -0.37$, $p < 0.01$). Moreover, correlations with local precipitation amounts are weak for both $\delta^{18}O$ ($r = -0.31$, $p < 0.01$) and *d*-excess ($r = 0.26$, $p < 0.01$). These findings lead us to infer that vapor isotopes during the summer monsoon season at the SETP are influenced by not only local precipitation–vapor interactions but also the history of precipitation–vapor interactions that occurred before the vapor reached the region.

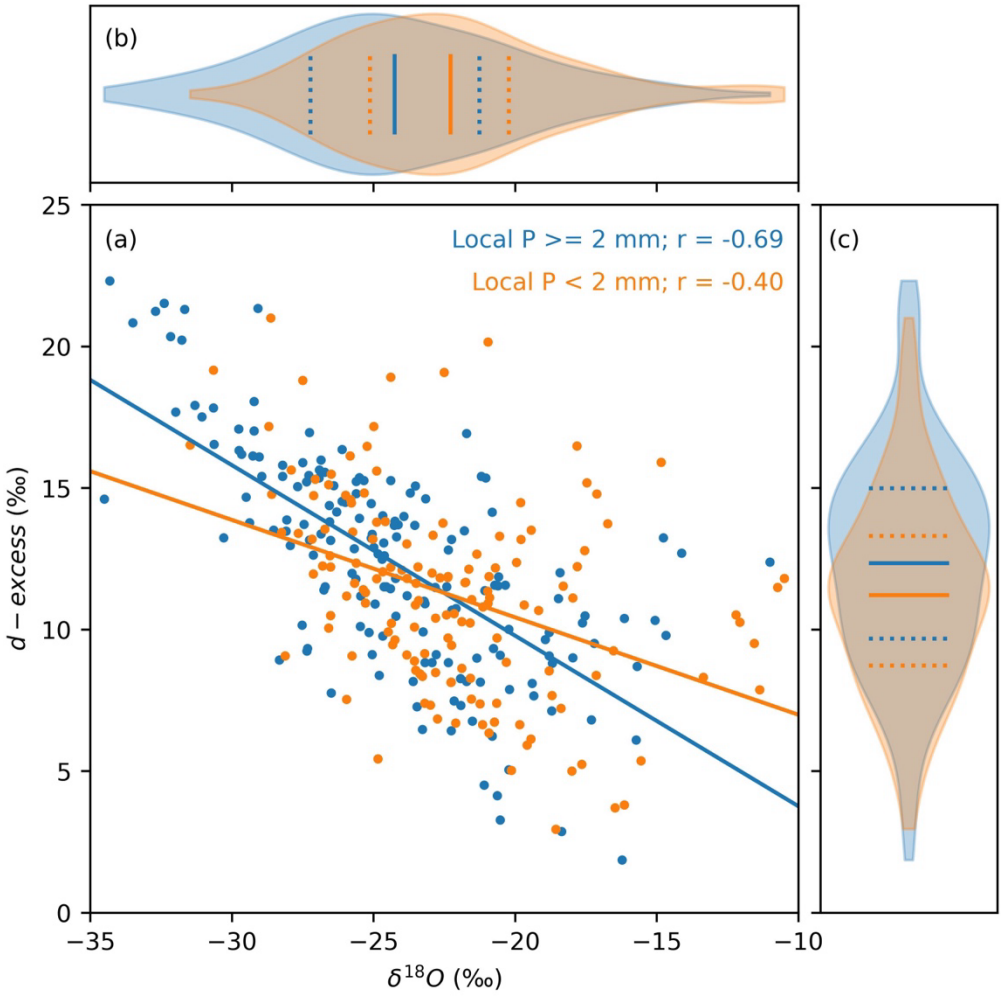

Figure 9: Relationships between SETP vapor *d*-excess and $\delta^{18}O$ during the summer monsoon season. (a) Scatter plot of *d*-excess against $\delta^{18}O$ and linear regression lines between them. (b) Distribution of $\delta^{18}O$ values, with the dashed lines indicating values at the lower and upper quartiles and the solid lines indicating the mean values. (c) Same as (b) but for *d*-excess. Orange colors indicate data observed when the daily precipitation amount is less than 2 mm, and blue colors indicate data observed during days when the precipitation amount is not less than 2 mm. The r values for both lines are indicated in (a), and both are significant at the 0.01 level.

To further investigate the role of precipitation–vapor interactions, we use the total precipitation amount (P_{acc}) as an indicator of precipitation–vapor interactions, considering the cumulative effect over several days preceding sampling. Our analysis examined correlations between vapor isotopes ($\delta^{18}O$ and *d*-excess) and P_{acc} over periods ranging from 1–10 days prior to sampling (Figs. S10 and S11). Vapor *d*-excess reaches an optimal correlation with P_{acc} when it is considered 3 days before sampling (P_{acc_3d}). Vapor $\delta^{18}O$ shows a slightly longer memory and reaches an optimal correlation approximately 5–6 days before sampling. Figure 10 shows the spatial distribution of these correlations, where *d*-excess positively correlates with P_{acc_3d} across an approximately 5°×5° region surrounding the SETP and extending southwestward to the Himalayas (Fig. 10a). In contrast, $\delta^{18}O$ values show significant negative correlations in similar regions (Fig. 10b). Interestingly, even on non-rainy days, significant regional-scale correlations persist, albeit weaker and with a smaller spatial extent (Fig. S12).

These findings provide further insights into understanding the mechanisms driving the amount effect. A negative correlation between $\delta^{18}O$ and P_{acc} has also been observed in precipitation and can be attributed to either continuous rainout (Kurita et al.,

2015; Cai and Tian, 2016; Ruan et al., 2019) or precipitation–vapor interactions (Lawrence et al., 2004; Worden et al., 2007; Risi et al., 2008a; Kurita et al., 2011). Although continuous rainout, explained by the Rayleigh distillation model, accounts for the decreasing trend of $\delta^{18}O$ with increased rainfall, *d*-excess remains relatively stable unless the specific humidity decreases to very low levels (approximately 4 g kg^{-1} in Fig. 3b, for example). The positive correlation between vapor *d*-excess and P_{acc_3d} provides an additional constraint, suggesting that the amount effect is not solely a result of rainout but also involves precipitation–vapor interactions, which significantly influence vapor isotopes in the lower troposphere.

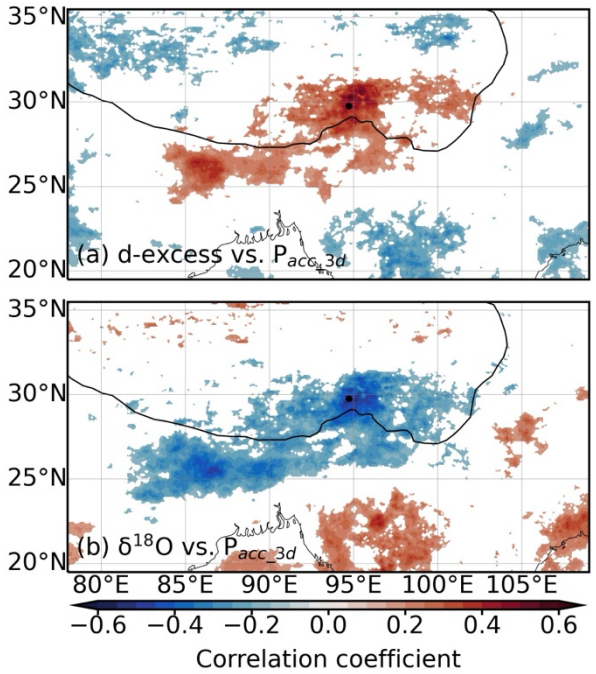

Figure 10: Relationships between vapor isotopes for rainy days (local daily precipitation amount not less than 2 mm) and total precipitation amount at the regional scale during the summer monsoon season. (a) Spatial distribution of correlation coefficients between *d*-excess and total precipitation amount during the 3 days prior to sampling (P_{acc_3d}). (b) Same as (a) but for $\delta^{18}O$. Only values significant at the 95% significance level are shown. The black dots indicate the location of the SETP station. The black solid lines denote the Tibetan Plateau with an altitude contour at 3000 m.

4 Implications for interpreting TP ice core isotope data

Interpreting *d*-excess in meteoric water and ice cores on the TP is complicated by evaporation conditions over the northern Indian Ocean (RH_{SST} and SST) and continental recycling (Pang et al., 2012; Zhao et al., 2012; Joswiak et al., 2013; An et al., 2017; Shao et al., 2021). Attempts have been made to establish relationships between vapor *d*-excess and RH_{SST} (Chen et al., 2024; Liu et al., 2024), as well as between ice core *d*-excess and RH_{SST} (Shao et al., 2021) or SST (Zhao et al., 2012). However, based on our results (Section 3.3), the apparent relationships are primarily a result of similarities in the seasonality of these variables. The preservation of oceanic source region conditions by vapor *d*-excess has also been questioned at other continental sites (Welp et al., 2012; Aemisegger et al., 2014; Samuels‐Crow et al., 2014; Fiorella et al., 2018; Wei and Lee, 2019). Instead, these studies emphasized the roles of other processes, such as continental recycling and mixing with subsiding air masses. For example, Aemisegger et al. (2014) suggested that high transpiration contributions could lead to a lack of correlations between

d-excess and RH_{SST}, as transpiration is non-fractionating under the steady-state assumption (Yakir and Sternberg, 2000). In addition, uncertainties associated with trajectory calculations and moisture source diagnostics, especially the resolution of the driven data, could also have an impact on the relationship between *d*-excess and RH_{SST}. While our study employs nested ERA5 and GDAS data with a resolution of 0.25°×0.25° from ERA5 in key moisture source regions, using coarser GDAS data does not alter our conclusions (not shown). However, higher-resolution data or regional high-resolution models could enhance the accuracy of trajectory calculations and reduce uncertainties.

The direct contribution of oceanic vapor to humidity at the SETP is very limited (Fig. 4), implying an even smaller contribution over the TP, as the SETP is at the forefront of moisture transport toward the TP (Fig. S1). The dominant terrestrial origin indicates significant continental recycling. Terrestrial processes such as transpiration and evaporation introduce isotopically enriched moisture with high *d*-excess signatures. Interestingly, vapor $\delta^{18}O$ exhibits a noticeable positive correlation with the fraction of within-boundary-layer moisture contribution over land during the non-monsoon season ($r = 0.47$, $p < 0.01$), suggesting that enhanced continental recycling would increase the $\delta^{18}O$ values (Fig. 3a). However, correlations between the fraction of terrestrial moisture sources and $\delta^{18}O$ for other seasons or with *d*-excess are either insignificant or marginal (Table S1). Further quantification of the effects of continental recycling on vapor isotopes requires detailed knowledge of the isotopic compositions of evapotranspiration fluxes. In this study, we utilized a simplified assumption regarding the isotopic composition of these fluxes to explore their influence on vapor isotopes. Therefore, future research should prioritize characterizing the isotopic signatures of both evaporation and transpiration fluxes, as well as determining the ratio between these two fluxes. This will provide deeper insights into how continental recycling shapes vapor isotope compositions.

Seasonal changes and long-term variations in precipitation and ice core isotopes have been interpreted as shifts in moisture sources between recycled terrestrial moisture and oceanic sources or their relative contributions (An et al., 2017; Yang and Yao, 2020). Oceanic moisture is typically associated with the summer monsoon, whereas westerlies bring moisture from continental recycling or even the Mediterranean Sea. Water isotopic signatures on the TP are thought to reflect this interplay between the summer monsoon and non-monsoon seasons (Tian et al., 2007; Pang et al., 2012; Joswiak et al., 2013). Despite seasonal shifts in moisture sources, continental recycling prevails throughout the year (Fig. 4). Our alternative perspective explains the high *d*-excess induced by westerlies as dry and cold air intrusions rather than surface evaporation or evapotranspiration. Although the interplay between the summer monsoon and westerlies remains valid, but we emphasize changes in air mass properties driven by different circulation systems.

The proposed alternative interpretation aligns with findings from the Andes (Samuels‐Crow et al., 2014) and Corsica (Sodemann et al., 2017), potentially explaining the abnormally high *d*-excess in high-altitude ice cores, as mentioned in the Introduction. This is because the specific humidity at these ice core sites is extremely low, and prolonged interactions with cold and dry air may further modify snow isotope compositions (Wahl et al., 2022; Ma et al., 2024). In addition, intense precipitation–vapor interactions during the summer monsoon represent another potential source of elevated *d*-excess (Section

3.5). When this high *d*-excess vapor contributes to subsequent precipitation, its signal can be inherited in the resulting precipitation (Risi et al., 2008b). However, a clear relationship between TP precipitation *d*-excess and monsoon convection has yet to be established, partly because of the limited attention given to *d*-excess in previous studies (Yao et al., 2013). Local raindrop evaporation may counteract this effect by reducing raindrop *d*-excess values. The overall positive correlation between precipitation *d*-excess and altitude across Asia has sometimes been attributed to stronger evaporation at lower altitudes (Bershaw, 2018). For snowfall on glaciers, however, evaporation from falling snowflakes is less likely due to cold temperatures and the short distance between the cloud base and the glacier surface. Therefore, elevated vapor *d*-excess values caused by accumulated precipitation–vapor interactions upstream associated with monsoon convection could be another source of the high *d*-excess values in ice cores.

5 Conclusions

We present a three-year daily near-surface vapor isotope dataset collected at the SETP station, which is at the major channel for moisture entering the TP. The paired measurements of vapor isotopes and specific humidity reveal distinct moisture sources and dynamics between the non-monsoon and summer monsoon seasons, which is consistent with the findings from the Lagrangian moisture diagnostic method. Despite significant negative correlations between *d*-excess and normalized RH over the northern Indian Ocean when all seasons are considered, these correlations weaken or even disappear when analyzed within individual seasons.

During the non-monsoon season, vapor *d*-excess is influenced primarily by specific humidity at both local and upstream scales. Air that has undergone significant dehydration, situated at the lower end of the Rayleigh distillation, is expected to have extremely high *d*-excess values. Backward trajectory analyses and moisture source diagnostics reveal that the intrusion of cold and dry air driven by westerlies during the non-monsoon season leads to an increasing trend in the *d*-excess as the specific humidity decreases. This process also contributes to a weak negative correlation between *d*-excess and $\delta^{18}O$. Furthermore, compared with the summer monsoon season, $\delta^{18}O$ primarily reflects mixing processes involving a relatively enriched moist end-member.

During the summer monsoon season, rain evaporation and “super-Rayleigh” processes emerge as the dominant processes shaping vapor isotope compositions. First, $\delta^{18}O$ systematically shifts below the Rayleigh distillation curve, aligning with predictions of “super-Rayleigh” distillation caused by partial rain evaporation. Second, $\delta^{18}O$ is inversely correlated with *d*-excess, indicating that kinetic fractionation is a source of depleted vapor, which cannot be attributed solely to rainout. Third, at the regional scale, $\delta^{18}O$ is significantly negatively correlated with the total precipitation amount, whereas *d*-excess is positively correlated with the total precipitation amount.

These findings will aid in interpreting $\delta^{18}O$ and *d*-excess records from Tibetan Plateau glaciers, offering refined insights into

past hydroclimatic conditions and challenging assumptions linking ice core isotopes to oceanic evaporation alone. These new insights into vapor *d*-excess during the non-monsoon season provide an alternative framework for interpreting the high *d*-excess values in high-altitude TP ice cores. The introduction of high *d*-excess values by subsidence air from high altitudes could be a general phenomenon, as similar findings have been reported elsewhere (Samuels‐Crow et al., 2014; Sodemann et al., 2017). Additionally, the findings on summer monsoon season moisture dynamics help disentangle the different effects of rainout and precipitation–vapor interactions in the context of the amount effect (Galewsky et al., 2016; Bowen et al., 2019). Although this study questions the earlier interpretation of TP *d*-excess as an indicator of oceanic evaporation conditions (Zhao et al., 2012; Shao et al., 2021; Chen et al., 2024; Liu et al., 2024), other studies have also raised doubts about the preservation of these signals inland (Welp et al., 2012; Aemisegger et al., 2014; Samuels‐Crow et al., 2014; Fiorella et al., 2018; Wei and Lee, 2019). Further research is needed to determine how far inland oceanic evaporation signals can be preserved during the transport from coastal areas. Moreover, we acknowledge the use of simplistic assumptions regarding the isotopic compositions of evapotranspiration fluxes, highlighting the need for deeper investigations into the isotopic compositions of these fluxes to comprehend the effects of continental recycling. Furthermore, the focus on lower tropospheric vapor sources contrasts with that on precipitation sources at higher levels, which may differ and require additional exploration. Finally, the resolution of meteorological data may influence the accuracy of trajectory calculations and moisture tracking results. Future research should consider the use of higher-resolution meteorological data or the implementation of regional high-resolution models to increase the precision of these analyses.

Competing interests

The authors declare that they have no conflict of interest.

Acknowledgements

We thank the editors and the referees for their comments and suggestions. We would like to thank the staff at the South-East Tibetan Plateau Station for integrated observation and research of alpine environment for their help in collecting water samples and for sharing the meteorological data at the station.

Financial support

This research was supported by the National Key R&D Program of China (Grant 2024YFF0807901), the National Natural Science Foundation of China (Grant 42371144), the Yunnan Fundamental Research Projects (Grant 202301AT070183), and the funding of Donglu Talent Young Scholar from the Yunnan University and support for young scholars from the Double First-Class Initiative for Ecological Disciplines of the Yunnan University.

Data availability

The NOAA ARL provided the HYSPLIT model and the GDAS data (https://www.ready.noaa.gov/HYSPLIT.php). The Copernicus Climate Change Service provided the ERA5 data (https://doi.org/10.24381/cds.adbb2d47 and https://doi.org/10.24381/cds.f17050d7). The GPM data are available through GES DISC (https://doi.org/10.5067/GPM/IMERG/3B-HH/07). Local meteorological data at the SETP station are provided by National Tibetan Plateau / Third Pole Environment Data Center (https://dx.doi.org/10.11888/AtmosphericPhysics.tpe.68.db). The observation data at the SETP station have been uploaded to Figshare and will be made publicly available after publication (10.6084/m9.figshare.27302871).

Author contributions

ZC: Conceptualization, methodology, investigation, formal analysis, funding acquisition, writing-original draft, writing-review & editing; **RL**: Investigation, data curation, writing-review & editing; **CW**: Validation; **QM**: Investigation, **LT**: Resources, project administration, funding acquisition.

References

Aemisegger, F., Pfahl, S., Sodemann, H., Lehner, I., Seneviratne, S. I., and Wernli, H.: Deuterium excess as a proxy for continental moisture recycling and plant transpiration, Atmos. Chem. Phys., 14, 4029-4054, https://doi.org/10.5194/acp-14-4029-2014, 2014.

An, W., Hou, S., Zhang, Q., Zhang, W., Wu, S., Xu, H., Pang, H., Wang, Y., and Liu, Y.: Enhanced Recent Local Moisture Recycling on the Northwestern Tibetan Plateau Deduced From Ice Core Deuterium Excess Records, J. Geophys. Res., 122, 12,541-512,556, https://doi.org/10.1002/2017jd027235, 2017.

Araguás-Araguás, L., Fröehlich, K., and Rozanski, K.: Stable isotope composition of precipitation over southeast Asia, J. Geophys. Res., 103, 28721-28742, 1998.

Benetti, M., Reverdin, G., Pierre, C., Merlivat, L., Risi, C., Steen-Larsen, H. C., and Vimeux, F.: Deuterium excess in marine water vapor: Dependency on relative humidity and surface wind speed during evaporation, J. Geophys. Res., 119, 584-593, 2014.

Bershaw, J.: Controls on Deuterium Excess across Asia, Geosciences, 8, 257, https://doi.org/10.3390/geosciences8070257, 2018.

Bonne, J.-L., Behrens, M., Meyer, H., Kipfstuhl, S., Rabe, B., Schönicke, L., Steen-Larsen, H. C., and Werner, M.: Resolving the controls of water vapour isotopes in the Atlantic sector, Nature Communications, 10, 1632,

https://doi.org/10.1038/s41467-019-09242-6, 2019.

Bonne, J. L., Masson-Delmotte, V., Cattani, O., Delmotte, M., Risi, C., Sodemann, H., and Steen-Larsen, H. C.: The isotopic composition of water vapour and precipitation in Ivittuut, southern Greenland, Atmos. Chem. Phys., 14, 4419-4439, https://doi.org/10.5194/acp-14-4419-2014, 2014.

Bony, S., Risi, C., and Vimeux, F.: Influence of convective processes on the isotopic composition ($\delta^{18}O$ and δD) of precipitation and water vapor in the tropics: 1. Radiative-convective equilibrium and Tropical Ocean–Global Atmosphere–Coupled Ocean-Atmosphere Response Experiment (TOGA-COARE) simulations, J. Geophys. Res., 113, D19305, https://doi.org/10.1029/2008JD009942, 2008.

Bowen, G. J. and Wilkinson, B.: Spatial distribution of $\delta^{18}O$ in meteoric precipitation, Geology, 30, 315, https://doi.org/10.1130/0091-7613(2002)030<0315:sdooim>2.0.co;2, 2002.

Bowen, G. J., Cai, Z., Fiorella, R. P., and Putman, A.: Isotopes in the Water Cycle: Regional- to Global-Scale Patterns and Applications, Annu. Rev. Earth Planet. Sci., 47, 453-479, https://doi.org/10.1146/annurev-earth-053018-060220, 2019.

Breitenbach, S. F. M., Adkins, J. F., Meyer, H., Marwan, N., Kumar, K. K., and Haug, G. H.: Strong influence of water vapor source dynamics on stable isotopes in precipitation observed in Southern Meghalaya, NE India, Earth Planet. Sci. Lett., 292, 212-220, https://doi.org/10.1016/j.epsl.2010.01.038, 2010.

Cai, Z. and Tian, L.: Atmospheric controls on seasonal and interannual variations in the precipitation isotope in the East Asian Monsoon region, J. Climate, 29, 1339-1352, https://doi.org/10.1175/JCLI-D-15-0363.1, 2016.

Cai, Z. and Tian, L.: What causes the post-monsoon ^{18}O depletion over Bay of Bengal head and beyond?, Geophys. Res. Lett., 47, e2020GL086985, https://doi.org/10.1029/2020gl086985, 2020.

Cai, Z., Tian, L., and Bowen, G. J.: ENSO variability reflected in precipitation oxygen isotopes across the Asian Summer Monsoon region, Earth Planet. Sci. Lett., 475, 25-33, https://doi.org/10.1016/j.epsl.2017.06.035, 2017.

Cai, Z., Tian, L., and Bowen, G. J.: Spatial-seasonal patterns reveal large-scale atmospheric controls on Asian Monsoon precipitation water isotope ratios, Earth Planet. Sci. Lett., 503, 158-169, https://doi.org/10.1016/j.epsl.2018.09.028, 2018.

Cai, Z., Li, R., Wang, C., and Tian, L.: Atmospheric controls on precipitation isotopes in North China and their response to record-breaking torrential rainfall, J. Hydrol., 661, 133762, https://doi.org/10.1016/j.jhydrol.2025.133762, 2025.

Cao, R., Huang, H., Wu, G., Han, D., Jiang, Z., Di, K., and Hu, Z.: Spatiotemporal variations in the ratio of transpiration to evapotranspiration and its controlling factors across terrestrial biomes, Agr. Forest Meteorol., 321, 108984, https://doi.org/10.1016/j.agrformet.2022.108984, 2022.

Chen, M., Gao, J., Luo, L., Zhao, A., Niu, X., Yu, W., Liu, Y., and Chen, G.: Temporal variations of stable isotopic compositions in atmospheric water vapor on the Southeastern Tibetan Plateau and their controlling factors, Atmos. Res., 303,

https://doi.org/10.1016/j.atmosres.2024.107328, 2024.

Craig, H.: Isotopic Variations in Meteoric Waters, Science, 133, 1702-1703, https://doi.org/10.1126/science.133.3465.1702, 1961.

Craig, H. and Gordon, L. I.: Deuterium and oxygen 18 variations in the ocean and the marine atmosphere, in: Stable Isotopes in Oceanographic Studies and Paleotemperatures. Spoleto, Tongiorgi, E., Italy, 9-130, 1965.

Dai, D., Gao, J., Steen-Larsen, H. C., Yao, T., Ma, Y., Zhu, M., and Li, S.: Continuous monitoring of the isotopic composition of surface water vapor at Lhasa, southern Tibetan Plateau, Atmos. Res., 264, https://doi.org/10.1016/j.atmosres.2021.105827, 2021.

Dansgaard, W.: Stable isotopes in precipitation, Tellus, 16, 436-468, https://doi.org/10.1111/j.2153-3490.1964.tb00181.x, 1964.

Dütsch, M., Pfahl, S., and Sodemann, H.: The impact of nonequilibrium and equilibrium fractionation on two different deuterium excess definitions, J. Geophys. Res., 122, 12732-12746, https://doi.org/10.1002/2017JD027085, 2017.

Fiorella, R. P., Poulsen, C. J., and Matheny, A. M.: Seasonal Patterns of Water Cycling in a Deep, Continental Mountain Valley Inferred from Stable Water Vapor Isotopes, J. Geophys. Res., 123, 7271-7291, https://doi.org/doi:10.1029/2017JD028093, 2018.

Galewsky, J., Steen-Larsen, H. C., Field, R. D., Worden, J., Risi, C., and Schneider, M.: Stable isotopes in atmospheric water vapor and applications to the hydrologic cycle, Rev. Geophys., 54, 809-865, https://doi.org/10.1002/2015RG000512, 2016.

Good, S. P., Noone, D., and Bowen, G.: Hydrologic connectivity constrains partitioning of global terrestrial water fluxes, Science, 349, 175-177, https://doi.org/10.1126/science.aaa5931, 2015.

Guo, H., Pang, H., Wu, S., Xu, T., Mutz, S. G., Zhan, Z., Lin, W., Zhang, W., and Hou, S.: Global abnormal precipitation ^{18}O depletion during late/post monsoon season, Earth Planet. Sci. Lett., 641, https://doi.org/10.1016/j.epsl.2024.118815, 2024.

Han, J., Tian, L., Cai, Z., Ren, W., Liu, W., Li, J., and Tai, J.: Season-specific evapotranspiration partitioning using dual water isotopes in a Pinus yunnanensis ecosystem, southwest China, J. Hydrol., 608, 127672, https://doi.org/10.1016/j.jhydrol.2022.127672, 2022.

He, S., Jackisch, D., Feng, L., Samanta, D., Wang, X., and Goodkin, N. F.: Uncovering Below Cloud Rain-Vapor Interactions During Tropical Rain Events Through Simultaneous and Continuous Real-Time Monitoring of Rain and Vapor Isotopes, J. Geophys. Res., 129, e2023JD040084, https://doi.org/10.1029/2023JD040084, 2024.

He, Y., Risi, C., Gao, J., Masson-Delmotte, V., Yao, T., Lai, C.-T., Ding, Y., Worden, J., Frankenberg, C., Chepfer, H., and Cesana, G.: Impact of atmospheric convection on south Tibet summer precipitation isotopologue composition using a combination of in situ measurements, satellite data and atmospheric general circulation modeling, J. Geophys. Res., 120, 3852-3871, https://doi.org/10.1002/2014JD022180, 2015.

Hersbach, H., Bell, B., Berrisford, P., Horányi, A., J., M.-S., Nicolas, J., Radu, R., Schepers, D., Simmons, A., Soci, C., and Dee, D.: Global reanalysis: goodbye ERA-Interim, hello ERA5, 10.21957/vf291hehd7, 2019.

Huang, J.: A Simple Accurate Formula for Calculating Saturation Vapor Pressure of Water and Ice, Journal of Applied Meteorology and Climatology, 57, 1265-1272, https://doi.org/JAMC-D-17-0334.1, 2018.

Huffman, G. J., Stocker, E. F., Bolvin, D. T., Nelkin, E. J., and Tan, J.: GPM IMERG Final Precipitation L3 Half Hourly 0.1 degree x 0.1 degree V07, Greenbelt, MD, Goddard Earth Sciences Data and Information Services Center (GES DISC) [dataset], https://doi.org/10.5067/GPM/IMERG/3B-HH/07, 2023.

Immerzeel, W. W., Lutz, A. F., Andrade, M., Bahl, A., Biemans, H., Bolch, T., Hyde, S., Brumby, S., Davies, B. J., Elmore, A. C., Emmer, A., Feng, M., Fernández, A., Haritashya, U., Kargel, J. S., Koppes, M., Kraaijenbrink, P. D. A., Kulkarni, A. V., Mayewski, P. A., Nepal, S., Pacheco, P., Painter, T. H., Pellicciotti, F., Rajaram, H., Rupper, S., Sinisalo, A., Shrestha, A. B., Viviroli, D., Wada, Y., Xiao, C., Yao, T., and Baillie, J. E. M.: Importance and vulnerability of the world's water towers, Nature, 577, 364-369, https://doi.org/10.1038/s41586-019-1822-y, 2020.

Jiang, J., Zhou, T., Qian, Y., Li, C., Song, F., Li, H., Chen, X., Zhang, W., and Chen, Z.: Precipitation regime changes in High Mountain Asia driven by cleaner air, Nature, https://doi.org/10.1038/s41586-023-06619-y, 2023.

Joswiak, D. R., Yao, T., Wu, G., Tian, L., and Xu, B.: Ice-core evidence of westerly and monsoon moisture contributions in the central Tibetan Plateau, J. Glaciol., 59, 56-66, https://doi.org/10.3189/2013JoG12J035, 2013.

Keeling, C. D.: The concentration and isotopic abundances of atmospheric carbon dioxide in rural areas, Geochim. Cosmochim. Acta, 13, 322-334, https://doi.org/10.1016/0016-7037(58)90033-4, 1958.

Kurita, N., Fujiyoshi, Y., Nakayama, T., Matsumi, Y., and Kitagawa, H.: East Asian Monsoon controls on the inter-annual variability in precipitation isotope ratio in Japan, Climate of the Past, 11, 339-353, https://doi.org/10.5194/cp-11-339-2015, 2015.

Kurita, N., Noone, D., Risi, C., Schmidt, G. A., Yamada, H., and Yoneyama, K.: Intraseasonal isotopic variation associated with the Madden-Julian Oscillation, J. Geophys. Res., 116, D24101, https://doi.org/10.1029/2010JD015209, 2011.

Lawrence, J. R., Gedzelman, S. D., Dexheimer, D., Cho, H.-K., Carrie, G. D., Gasparini, R., Anderson, C. R., Bowman, K. P., and Biggerstaff, M. I.: Stable isotopic composition of water vapor in the tropics, J. Geophys. Res., 109, D06115, https://doi.org/10.1029/2003JD004046, 2004.

Lee, J.-E. and Fung, I.: "Amount effect" of water isotopes and quantitative analysis of post-condensation processes, Hydrol. Processes, 22, 1-8, https://doi.org/10.1002/hyp.6637, 2008.

Li, R., Cai, Z., Wang, C., Liu, F., Yang, D., Xu, C., Yu, S., Yu, X., Fan, Q., and Tian, L.: Multiple Climate Forcings Decomposed From a Tibetan Plateau Ice Core Isotope Record, J. Geophys. Res., 130, e2024JD042929, https://doi.org/10.1029/2024JD042929, 2025.

Liu, F., Tian, L., Cai, Z., Wang, X., Liang, P., Wang, S., and Li, S.: What caused the lag between oxygen-18 and deuterium

excess in atmospheric vapor and precipitation during the earlier summer season in southwest China?, J. Hydrol., 644, https://doi.org/10.1016/j.jhydrol.2024.132087, 2024.

Liu, J., Xiao, C., Ding, M., and Ren, J.: Variations in stable hydrogen and oxygen isotopes in atmospheric water vapor in the marine boundary layer across a wide latitude range, Journal of Environmental Sciences, 26, 2266-2276, https://doi.org/10.1016/j.jes.2014.09.007, 2014.

Luo, L.: Meteorological observation data from the integrated observation and research station of the alpine environment in Southeast Tibet (2007-2017), National Tibetan Plateau Data Center [dataset], https://doi.org/10.11888/AtmosphericPhysics.tpe.68.db, 2018.

Ma, T., Jiang, Z., Ding, M., He, P., Li, Y., Zhang, W., and Geng, L.: A model framework for atmosphere–snow water vapor exchange and the associated isotope effects at Dome Argus, Antarctica – Part 1: The diurnal changes, The Cryosphere, 18, 4547-4565, https://doi.org/10.5194/tc-18-4547-2024, 2024.

Merlivat, L. and Jouzel, J.: Global climatic interpretation of the deuterium-oxygen 18 relationship for precipitation, J. Geophys. Res., 84, 5029-5033, 1979.

Noone, D.: Pairing Measurements of the Water Vapor Isotope Ratio with Humidity to Deduce Atmospheric Moistening and Dehydration in the Tropical Midtroposphere, J. Climate, 25, 4476-4494, https://doi.org/10.1175/jcli-d-11-00582.1, 2012.

Pang, H., Hou, S., Kaspari, S., Mayewski, P., Introne, D., Masson-Delmotte, V., Jouzel, J., Li, Z., He, Y., Hong, S., and Qin, D.: Atmospheric circulation change in the central Himalayas indicated by a high-resolution ice core deuterium excess record, Climate Research, 53, 1-12, https://doi.org/10.3354/cr01090, 2012.

Putman, A. L., Fiorella, R. P., Bowen, G. J., and Cai, Z.: A Global Perspective on Local Meteoric Water Lines: Meta-analytic Insight into Fundamental Controls and Practical Constraints, Water Resour. Res., 55, 6896-6910, https://doi.org/10.1029/2019wr025181, 2019.

Risi, C., Bony, S., and Vimeux, F.: Influence of convective processes on the isotopic composition ($\delta^{18}O$ and δD) of precipitation and water vapor in the tropics: 2. Physical interpretation of the amount effect, J. Geophys. Res., 113, D19306, https://doi.org/10.1029/2008JD009943, 2008a.

Risi, C., Bony, S., Vimeux, F., Descroix, L., Ibrahim, B., Lebreton, E., Mamadou, I., and Sultan, B.: What controls the isotopic composition of the African monsoon precipitation? Insights from event-based precipitation collected during the 2006 AMMA field campaign, Geophys. Res. Lett., 35, L24808, https://doi.org/10.1029/2008GL035920, 2008b.

Ruan, J., Zhang, H., Cai, Z., Yang, X., and Yin, J.: Regional controls on daily to interannual variations of precipitation isotope ratios in Southeast China: Implications for paleomonsoon reconstruction, Earth Planet. Sci. Lett., 527, 115794, https://doi.org/10.1016/j.epsl.2019.115794, 2019.

Samuels-Crow, K. E., Galewsky, J., Sharp, Z. D., and Dennis, K. J.: Deuterium excess in subtropical free troposphere water

vapor: Continuous measurements from the Chajnantor Plateau, northern Chile, Geophys. Res. Lett., 41, 8652-8659, https://doi.org/10.1002/2014gl062302, 2014.

Shao, L., Tian, L., Cai, Z., Wang, C., and Li, Y.: Large-scale atmospheric circulation influences the ice core d-excess record from the central Tibetan Plateau, Clim. Dyn., 57, 1805-1816, https://doi.org/10.1007/s00382-021-05779-9, 2021.

Sodemann, H.: The Lagrangian moisture source and transport diagnostic WaterSip V3.2, EGUsphere [preprint], https://doi.org/10.5194/egusphere-2025-574, 2025.

Sodemann, H., Schwierz, C., and Wernli, H.: Interannual variability of Greenland winter precipitation sources: Lagrangian moisture diagnostic and North Atlantic Oscillation influence, J. Geophys. Res., 113, https://doi.org/10.1029/2007jd008503, 2008.

Sodemann, H., Aemisegger, F., Pfahl, S., Bitter, M., Corsmeier, U., Feuerle, T., Graf, P., Hankers, R., Hsiao, G., Schulz, H., Wieser, A., and Wernli, H.: The stable isotopic composition of water vapour above Corsica during the HyMeX SOP1 campaign: insight into vertical mixing processes from lower-tropospheric survey flights, Atmos. Chem. Phys., 17, 6125-6151, https://doi.org/10.5194/acp-17-6125-2017, 2017.

Steen-Larsen, H. C., Risi, C., Werner, M., Yoshimura, K., and Masson-Delmotte, V.: Evaluating the skills of isotope-enabled General Circulation Models against in-situ atmospheric water vapor isotope observations, J. Geophys. Res., 122, 246-263, https://doi.org/10.1002/2016JD025443, 2017.

Stein, A. F., Draxler, R. R., Rolph, G. D., Stunder, B. J. B., Cohen, M. D., and Ngan, F.: NOAA's HYSPLIT atmospheric transport and dispersion modeling system, Bull. Am. Meteorol. Soc., 96, 2059-2077, https://doi.org/10.1175/BAMS-D-14-00110.1, 2015.

Terzer-Wassmuth, S., Wassenaar, L. I., Welker, J. M., and Araguas-Araguas, L. J.: Improved High-Resolution Global and Regionalized Isoscapes of $\delta^{18}O$, $\delta^{2}H$, and d-excess in Precipitation, Hydrol. Processes, 35, https://doi.org/10.1002/hyp.14254, 2021.

Thompson, L. G., Yao, T., E.Mosley-Thompson, Davis, M. E., Henderson, K. A., and Lin, P.-N.: A High-Resolution Millennial Record of the South Asian Monsoon from Himalayan Ice Cores, Science, 289, 1916-1919, https://doi.org/10.1126/science.289.5486.1916, 2000.

Thompson, L. G., Yao, T. D., Davis, M. E., Mosley-Thompson, E., Synal, H. A., Wu, G., Bolzan, J. F., Kutuzov, S., Beaudon, E., Sierra-Hernández, M. R., and Beer, J.: Ice core evidence for an orbital-scale climate transition on the Northwest Tibetan Plateau, Quat. Sci. Rev., 324, https://doi.org/10.1016/j.quascirev.2023.108443, 2024.

Tian, L., Masson-Delmotte, V., Stievenard, M., Yao, T., and Jouzel, J.: Tibetan Plateau summer monsoon northward extent revealed by measurements of water stable isotopes, J. Geophys. Res., 106, 28081-28088, https://doi.org/10.1029/2001JD900186, 2001.

Tian, L., Yao, T., MacClune, K., White, J. W. C., Schilla, A., Vaughn, B., Vachon, R., and Ichiyanagi, K.: Stable isotopic

variations in west China: A consideration of moisture sources, J. Geophys. Res., 112, D10112, https://doi.org/10.1029/2006jd007718, 2007.

Tian, L., Yu, W., Schuster, P. F., Wen, R., Cai, Z., Wang, D., Shao, L., Cui, J., and Guo, X.: Control of seasonal water vapor isotope variations at Lhasa, southern Tibetan Plateau, J. Hydrol., 580, 124237, https://doi.org/10.1016/j.jhydrol.2019.124237, 2020.

Uemura, R., Matsui, Y., Yoshimura, K., Motoyama, H., and Yoshida, N.: Evidence of deuterium excess in water vapor as an indicator of ocean surface conditions, J. Geophys. Res., 113, https://doi.org/10.1029/2008jd010209, 2008.

Wahl, S., Steen-Larsen, H. C., Hughes, A. G., Dietrich, L. J., Zuhr, A., Behrens, M., Faber, A.-K., and Hörhold, M.: Atmosphere-Snow Exchange Explains Surface Snow Isotope Variability, Geophys. Res. Lett., 49, e2022GL099529, https://doi.org/10.1029/2022GL099529, 2022.

Webster, C. R. and Heymsfield, A. J.: Water isotope ratios D/H, 18O/16O, 17O/16O in and out of clouds map dehydration pathways, Science, 302, 1742-1745, https://doi.org/10.1126/science.1089496, 2003.

Wei, Z. and Lee, X.: The utility of near-surface water vapor deuterium excess as an indicator of atmospheric moisture source, J. Hydrol., 123923, https://doi.org/10.1016/j.jhydrol.2019.123923, 2019.

Welp, L. R., Lee, X., Griffis, T. J., Wen, X. F., Xiao, W., Li, S., Sun, X., Hu, Z., Val Martin, M., and Huang, J.: A meta-analysis of water vapor deuterium-excess in the midlatitude atmospheric surface layer, Global Biogeochem. Cycles, 26, https://doi.org/10.1029/2011gb004246, 2012.

Worden, J., Noone, D., and Bowman, K.: Importance of rain evaporation and continental convection in the tropical water cycle, Nature, 445, 528-532, https://doi.org/10.1038/nature05508, 2007.

Yakir, D. and Sternberg, L. d. S. L. J. O.: The use of stable isotopes to study ecosystem gas exchange, 123, 297-311, https://doi.org/10.1007/s004420051016, 2000.

Yang, X. and Yao, T.: Seasonality of moisture supplies to precipitation over the Third Pole: a stable water isotopic perspective, Sci Rep, 10, 15020, https://doi.org/10.1038/s41598-020-71949-0, 2020.

Yang, X., Davis, M. E., Acharya, S., and Yao, T.: Asian monsoon variations revealed from stable isotopes in precipitation, Clim. Dyn., 51, 2267-2283, https://doi.org/10.1007/s00382-017-4011-4, 2017.

Yao, T., Masson-Delmotte, V., Gao, J., Yu, W., Yang, X., Risi, C., Sturm, C., Werner, M., Zhao, H., He, Y., Ren, W., Tian, L., Shi, C., and Hou, S.: A review of climatic controls on $\delta^{18}O$ in precipitation over the Tibetan Plateau: Observations and simulations, Rev. Geophys., 51, 525-548, https://doi.org/10.1002/rog.20023, 2013.

Yao, T., Bolch, T., Chen, D., Gao, J., Immerzeel, W., Piao, S., Su, F., Thompson, L., Wada, Y., Wang, L., Wang, T., Wu, G., Xu, B., Yang, W., Zhang, G., and Zhao, P.: The imbalance of the Asian water tower, Nature Reviews Earth & Environment, 3, 618-632, https://doi.org/10.1038/s43017-022-00299-4, 2022.

Yu, W., Tian, L., Ma, Y., Xu, B., and Qu, D.: Simultaneous monitoring of stable oxygen isotope composition in water vapour

and precipitation over the central Tibetan Plateau, Atmos. Chem. Phys., 15, 10251-10262, https://doi.org/10.5194/acp-15-10251-2015, 2015.

Yu, W., Tian, L., Risi, C., Yao, T., Ma, Y., Zhao, H., Zhu, H., He, Y., Xu, B., Zhang, H., and Qu, D.: $\delta^{18}O$ records in water vapor and an ice core from the eastern Pamir Plateau: Implications for paleoclimate reconstructions, Earth Planet. Sci. Lett., 456, 146-156, https://doi.org/10.1016/j.epsl.2016.10.001, 2016.

Zhang, Q., Shen, Z., Pokhrel, Y., Farinotti, D., Singh, V. P., Xu, C.-Y., Wu, W., and Wang, G.: Oceanic climate changes threaten the sustainability of Asia's water tower, Nature, 615, 87-93, https://doi.org/10.1038/s41586-022-05643-8, 2023.

Zhang, Q., Shen, Z., Pokhrel, Y., Farinotti, D., Singh, V. P., Xu, C.-Y., Wu, W., and Wang, G.: Reply to: Atlantic oceanic droughts do not threaten Asian water tower, Nature, 638, E16-E18, https://doi.org/10.1038/s41586-024-08358-0, 2025.

Zhao, H., Xu, B., Li, Z., Wang, M., Li, J., and Zhang, X.: Abundant climatic information in water stable isotope record from a maritime glacier on southeastern Tibetan Plateau, Clim. Dyn., 48, 1161-1171, https://doi.org/10.1007/s00382-016-3133-4, 2017.

Zhao, H., Xu, B., Yao, T., Wu, G., Lin, S., Gao, J., and Wang, M.: Deuterium excess record in a southern Tibetan ice core and its potential climatic implications, Clim. Dyn., 38, 1791-1803, https://doi.org/10.1007/s00382-011-1161-7, 2012.

Zhao, Y., Xu, C., Yu, X., Liu, Y., and Ji, X.: Atlantic oceanic droughts do not threaten Asian water tower, Nature, 638, E13-E15, https://doi.org/10.1038/s41586-024-08357-1, 2025.